Characterizing the reactivation mechanisms of coseismic surface ruptures associated with the 2011 Mw 6.7 Fukushima-ken Hamadori earthquake in Japan through borehole hydromechanical testing

Yves Guglielmi, Kazuhiro Aoki, Paul Cook, Florian Soom, Frédéric Cappa, Yukumo Tanaka

To cite this version:

Yves Guglielmi, Kazuhiro Aoki, Paul Cook, Florian Soom, Frédéric Cappa, et al.. Characterizing the reactivation mechanisms of coseismic surface ruptures associated with the 2011 Mw 6.7 Fukushima-ken Hamadori earthquake in Japan through borehole hydromechanical testing. Tectonophysics, 2021, 819, pp.229084. 10.1016/j.tecto.2021.229084 . hal-03375052

HAL Id: hal-03375052
https://hal.science/hal-03375052v1

Submitted on 13 Oct 2021

Tectonophysics 819 (2021) 229084

Contents lists available at ScienceDirect

Tectonophysics

journal homepage: www.elsevier.com/locate/tecto

Characterizing the reactivation mechanisms of coseismic surface ruptures associated with the 2011 M_w 6.7 Fukushima-ken Hamadori earthquake in Japan through borehole hydromechanical testing

Yves Guglielmi [a,*], Kazuhiro Aoki [b], Paul Cook [a], Florian Soom [a], Frédéric Cappa [c], Yukumo Tanaka [b]

[a] *Lawrence Berkeley National Laboratory, Energy Geoscience Division, Berkeley, CA 94720, USA*
[b] *Japan Atomic Energy Agency, Department of Construction, Tokai-mura, Naka-gun, Ibaraki 319-1195, Japan*
[c] *Université Côte d'Azur, CNRS, Observatoire de la Côte d'Azur, IRD, Géoazur, Nice, France*

ARTICLE INFO

Keywords:
Coseismic surface rupture
Hydromechanical testing
Active fault Japan

ABSTRACT

The reactivation mechanisms of coseismic surface ruptures associated with the 2011 M_w 6.7 Fukushima-ken Hamadori earthquake in Japan are investigated using in-situ controlled hydraulic injections in subsurface boreholes. Two fault segments were selected for reactivation studies, one across a coseismic rupture, the Shionohira site, and one across a non-coseismically ruptured segment, the Minakami-kita site. A series of water injections in sealed sections of boreholes set across the fault progressively bring the fault to rupture by a step-by-step decrease of the effective normal stress clamping the fault. While the fault is rupturing during these hydraulic stimulations, borehole displacements, fluid pressure and injection flowrate are continuously monitored. Then, the tests were analyzed using fully coupled hydromechanical modeling. The model was calibrated on field data, and a parametric study was conducted to examine the modes of fault reactivation. Coseismic surface rupture of the Shionohira fault showed a pure dilatant slip response to hydraulic tests, while the tectonically un-activated Itozawa fault (South) indicated a complex hybrid response to tests related to both a higher frictional and cohesive strengths of the fault. The analysis of the induced Shionohira slip event showed that it is reasonably modeled as a Coulomb rupture with an eventual dependency of friction on slip velocity, in good accordance with laboratory-derived rate-and-state friction data on the Shinohira gouge samples. In contrast, the Itozawa fault reactivation mechanism appears dominated by tensile failure with limited Coulomb shear failure. Thus, the applied protocol proves to be able to isolate significant differences in fault physical properties and rupture mechanisms between two segments of the same fault system, opening perspectives to better assess near-surface rupture effects, and therefore the safety of structures such as dams or nuclear waste repositories subject to large earthquakes.

1. Introduction

In earthquake geology and mechanics, the characterization of surface deformation is crucial, especially when the coseismic rupture reaches the surface from the seismogenic depth (Anastasopoulos et al., 2007). The geometry of the rupture trace at the ground surface, rock mechanical properties and coseismic slip profiles can be used to refine the seismic sources models, and to better assess the seismic hazards. The conditions for fault slip to reach the ground surface are depending on the rupture mechanism, the stress conditions at depth and, the geology of subsurface rocks and complex stress perturbations close to the topographic surface (Avar and Hudyma, 2019). The presence of previous fault ruptures may influence the location of the more recent surface fault ruptures. Although the mechanism of fault rupture propagation to ground surface mainly depends on crustal geology and tectonics, field studies after earthquakes highlighted the effects of near-surface deposits, if they exist, on the width and architecture of the outcropping fault rupture. This is apparently truer in the case of reverse faults than in the case of normal or strike slip faults (Avar and Hudyma, 2019). The primary origin of the surface ruptures (i.e., surface ruptures due to slip on the fault responsible for seismic energy release) is thus sometimes difficult to demonstrate. This is one reason why multiple analyses may

---

* Corresponding author.
E-mail address: YGuglielmi@lbl.gov (Y. Guglielmi).

https://doi.org/10.1016/j.tecto.2021.229084
Received 7 January 2021; Received in revised form 9 September 2021; Accepted 25 September 2021

show that in general coseismic fault slip at the surface is less than slip at depth. One explanation is the velocity-strengthening behavior of the shallow faults (Scholz, 1998). Nevertheless, Noda and Lapusta (2013) highlighted that, if the dynamic weakening is activated, the coseismic slip at the surface could be larger than the slip at depth. Yet total slip which includes coseismic slip and aseismic slip at the surface tends to equal total slip at depth over multiple earthquake cycles. Dolan and Haravitch (2014) observed that such a deficit of apparent shallow slip was higher on immature fault zones (<25 km total displacement) where it may be accounted by off-fault distributed deformation.

The main mitigation approach of the hazard related to surface fault ruptures is to set infrastructures far enough from the active fault. This is usually done through a site-specific investigation aiming at identifying the fault location and whether or not this fault is active. Current investigations involve mapping fault traces, trenching to identify past activity from perturbations of the shallow sediments stratigraphy, coring to identify fault materials and eventually characterize their properties later at laboratory scale (Avar and Hudyma, 2019). Some shallow subsurface geophysics can also be deployed to image fault offset at depth. One of the main difficulties in site investigations is to determine whether the fault mapped at a trench is active or inactive. Hart et al. (1993) and Lienkaemper et al. (1991) showed that almost half of the new surface ruptures localize outside zones established from such investigations. Moreover, when no shallow sediments mark the fault offset (s), it is almost impossible to determine if the fault is potentially active.

Faults are several meter to hundreds of meter thick zones made of complex highly deformed fractured and low cohesive materials. It is usually considered that fault zones contain core zones where the largest shear displacements localize surrounded by a fractured damage zone (Mitchell and Faulkner, 2009). Such structural complexity induces a strong variability of fault zones hydromechanical properties that influence poroelastic behavior (Jeanne et al., 2014, 2017), state of stress (Barton and Zoback, 1994), fault frictional evolution and earthquake nucleation (Aki, 1995; Guglielmi et al., 2015a, 2015b; Cappa et al., 2019). For these reasons the characterization of fault properties at the meter to tens-of-meters scale, which is the proper fault zone scale in the field, and a better understanding of how these “field scale” fault properties influence the mode of fault activation are major issues in seismic

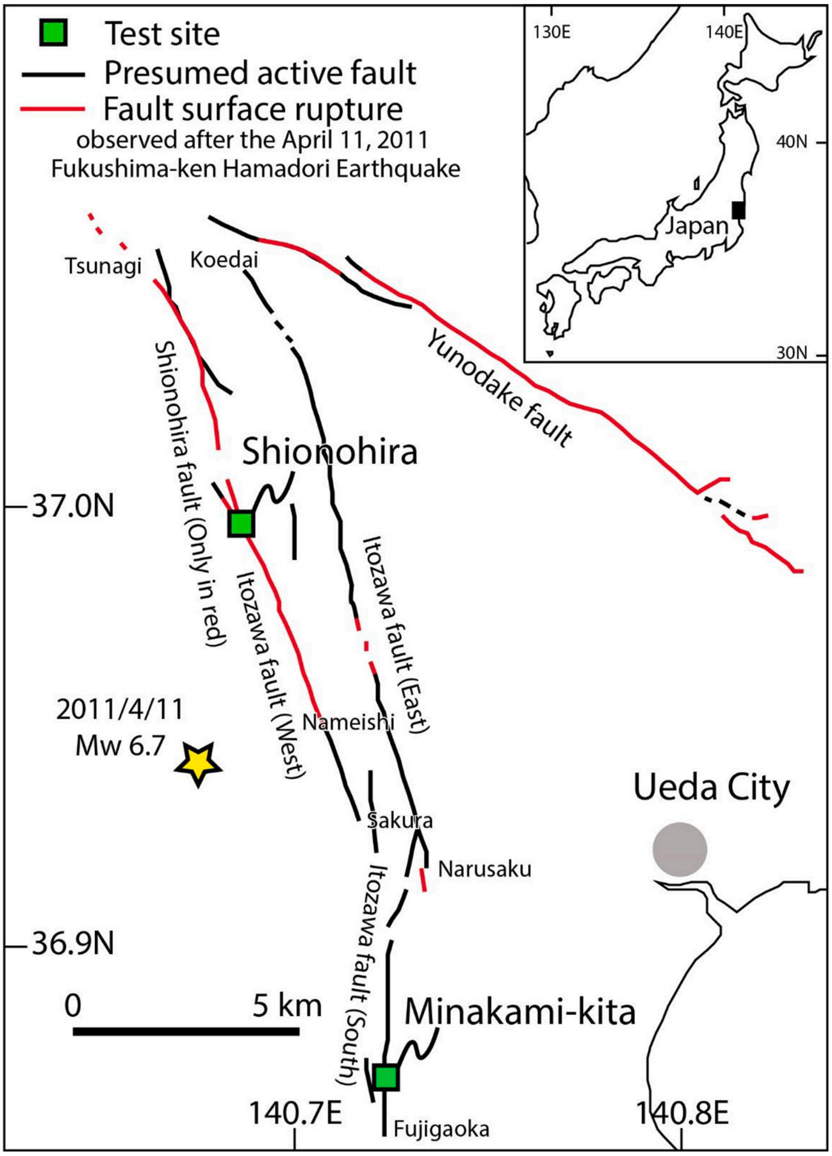

Fig. 1. Location of the test sites. Coseismic surface ruptures are shown in red colour. The yellow star is the location of the Fukushima-ken Hamadori Earthquake epicenter. Shinohira test site is located on the activated Shionohira fault, while Minakami-kita test site is located across the inactivated Itozawa fault (South). (For interpretation of the references to colour in this figure legend, the reader is referred to the web version of this article.)

risk assessment.

Here we focus on faults that were activated near the Pacific coast at the Ibaraki-Fukushima prefecture 1 month after the occurrence of the 2011 Mw 9.0 Tohoku-Oki earthquake (Fig. 1). A shallow normal faulting earthquake sequence occurred with roughly E–W or NW– SE extension direction, characterized by the April 11, 2011 Fukushima-ken Hamadori Earthquake of Mw 6.7 (Yoshida et al., 2015). In details, rupture initiated on the Itozawa fault propagating mainly up dip and NW (Tanaka et al., 2014). It then triggered a rupture on the Yunokade fault that first propagated up dip than DE at shallow depth. The earthquake caused surface ruptures characterized by westward dipping normal-fault scarps mapped along several segments of the Itozawa, Yunodake and Shionohira faults with average dip direction/dip angle of 260/70, and 2 m maximum displacement (Otsubo et al., 2013). The studied area originally had two faults mapped: the Yunodake fault and a few lineaments grouped together as the Itozawa fault. Both faults were interpreted to be potentially active without discernible slip sense (Research Group on Active Faults of Japan, 1991; Nakata and Imaizumi, 2002). Fukushima-ken Hamadori Earthquake of Mw 6.7 occurred on April 11, 2011, just 1 month after the Tohoku-oki Earthquake of Mw 9.0. Co-seismic surface ruptures appeared approximately 14 km along a part of the western section of NNW-SSE trending Itozawa fault and 15 km along the NW-SE trending Yunodake fault (shown in red colour in Fig. 1). Faint slips were recognized on the eastern section of the NNW-SSE trending Itozawa fault, but no rupture exposed along the southern section of N-S trending Itozawa fault. After the earthquake, Itozawa fault was recognized to be composed of three distinct sections based on aerial photograph interpretation: eastern, western and southern sections (Toda and Tsutsumi, 2013). The NNW-SSE trending eastern section (Itozawa fault (East) in Fig. 1) is straight and continuous from Koedai to Narusaku. The western section, extending from Tsunagi to Sakura, is parallel to the eastern section. The N-S trending southern section branches from the eastern section at Sakura and extends southward to Fujioka. The surface ruptured part from Tsunagi to Nameishi of the western section of Itozawa fault was newly named the Shionohira fault (Ishiyama et al., 2011). Shionohira test site is located on the activated Shionohira fault, while Minakami-kita test site is located across the inactivated Itozawa fault (South). The causes of faults activation might be related to changes in the stress state following the Tohoku-Oki earthquake (Kato et al., 2011). Here, we explore if differences in fault hydromechanical properties may explain that some fault segments were activated and ruptured the land surface while others remained inactive although being very close and aligned on the same fault zone.

In 2018 and 2019, we conducted hydraulic tests in shallow 20–30 m deep boreholes cross-cutting one activated of the Shionohira fault and one inactivated segment of the Itozawa fault (South), respectively at the Shionohira and at the Minakami-kita sites (Fig. 1). A borehole probe developed by LBNL (Lawrence Berkeley National Laboratory, Berkeley, US) was deployed, and the Step Rate Injection Method for Fracture InSitu Properties (SIMFIP, Guglielmi et al., 2014) was applied in borehole sealed-sections set across the fault zone. Basically, the key idea of the SIMFIP tests is to pressurize the fault zone in an interval isolated by inflatable packers until a micro-to-millimeter scale fault movement is triggered. We report here the first application of this instrument to the in situ hydromechanical characterization of a recently ruptured active fault in a shallow stress field environment. We first describe the experimental setting and the measured fault three-dimensional displacements and pore pressure variations during the tests. We then conduct a three-dimensional forward analysis of the fault hydromechanical response to explore the different parameters driving this local fault reactivation mechanism, including an estimate of the amount of shear slip triggered on the fault. We then use a one-dimensional inverse analysis of the slip events to evaluate the fault frictional dependency on slip velocity. Finally, we discuss how this new in situ testing protocol can help identifying differences in hydro-mechanical properties and in rupture mechanisms between an activated and un-activated fault segment, and better assessing the effects of fault surface rupture related to seismic events on the safety of human structures in Japan and in other countries.

2. Experimental setting

2.1. SIMFIP protocol for fault reactivation by fluid injection

The instrument used for the fault zone isolation is a double-packer probe instrumented with a high-resolution fiber-optic three-dimensional displacement borehole sensor and a fluid pressure sensor (Guglielmi et al., 2014 and Fig. 2). The SIMFIP method relies on hydraulic tests performed in boreholes with the probe. It has been deployed in several research experiments set in Underground Research Laboratories (URL) worldwide (Guglielmi et al., 2015a, 2015b). Since 2017, LBNL has developed different versions of the SIMFIP probes that

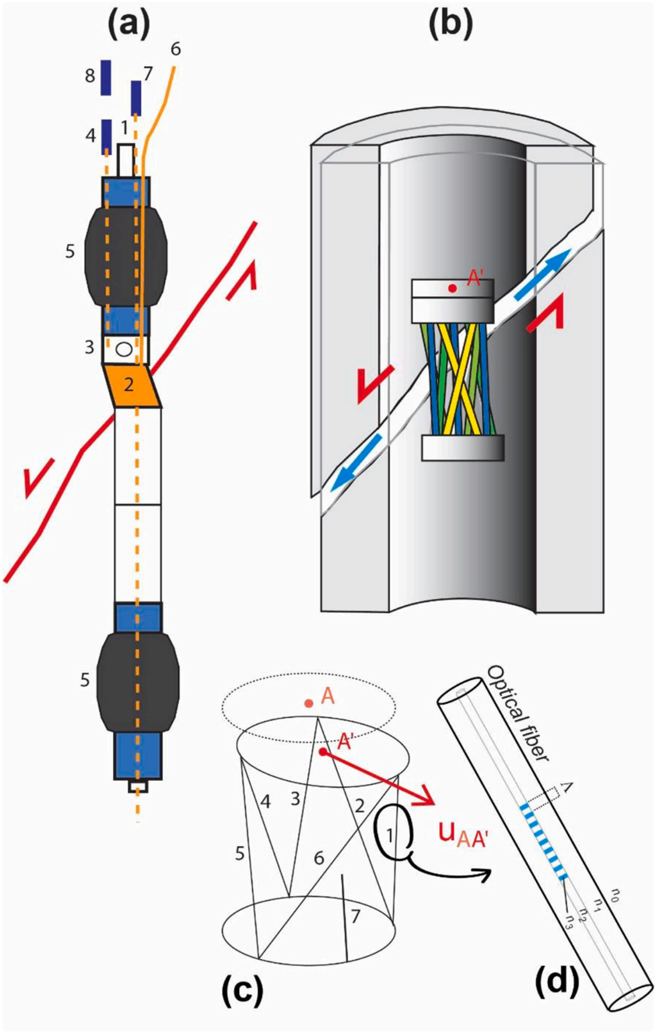

Fig. 2. SIMFIP probe. (a) Geometry of the entire probe (1 – Injection line, 2 – SIMFIP three dimensional sensor, 3 – Injection element allowing injection between the two packers, 4 – Injection chamber pressure sensor, 5 – Inflatable packers, 6 – Optical fiber connected to the SIMFIP cage, 7 – Pressure sensor controlling pressure below the lower packer, 8 – Pressure sensor controlling pressure above the upper packer); (b) Details of the SIMFIP cage (Colors show that depending on their orientation cage's wings deform differently while the fault is activated); (c) Schematic geometry of the SIMFIP cage which is measuring displacement of point A to A' (1–7 are the Bragg gratings); (c) Bragg grating corresponding to one of the 7 strain gauges probing the deformation of cage's wings 1–7. Strain gauge 7 is a reference FBG subject to ambient pressure and temperature which remains unstressed.

allow testing different fault thickness (up to ~5 m), soft and/or hard rock materials and at increased pressure/depth conditions up to 40 MPa. In this study, the SIMFIP three-dimensional displacement sensor which is a 0.2 m long and 0.1 m diameter pre-calibrated aluminum cage is integrated in the mandrel straddling the two 1 m long probe's inflatable rubber packers which are sliding sleeves (Fig. 2a). The packers play two roles, respectively, sealing the test interval in the borehole and anchoring the displacement sensor. When water pressure is increased in the sealed zone and the fault starts moving, the SIMFIP sensor monitors the displacement of the upper packer relative to the lower packer (Fig. 2b). The aluminum cage is instrumented with 6 strain measurements performed with optical Fiber Bragg Gratings (FBG) that are mechanically clamped on the 6 wings of the deforming cage (numbers 1–6 in Fig. 2c). Each FBG gage (Fig. 2d) measures the cage's strain in one uniaxial direction. Thus, the cage allows for 6 different uniaxial strain directions to be continuously monitored at high-frequency (~0.5 kHz) during the test. In addition, there is a reference FBG subject to ambient pressure and temperature which remains unstressed (number 7 in Fig. 2c). All the FBG are distributed along one single fiber that brings the sensor signals to a MicronOptics Si155 acquisition system set at the ground surface. This interrogator allows picking shifts in the FBG wavelength that relate to FBG deformation over a large spectrum of FBG wavelengths. The 6 components of the tensor describing the relative displacement and rotation between the top and bottom of the cage are calculated as a linear function of the 6 strain components.

The sequence of operation consists of the following steps. First, the fault zone is sealed in an open hole using the two inflatable rubber packers. The probe was adapted to each borehole-fault intersection geometry, the longer the intersection's length the longer the distance between the probe's packers (Fig. 3). Thus, the distance between packers is longer in Shinohira (Fig. 3a, b) compared to Minakami-kita (Fig. 3c, d), respectively of 4.5 and 1.95 m. Second, a series of fluid injections either at controlled constant pressure or constant flow rate are conducted. The key idea is to progressively bring the fault to rupture by a step-by-step decrease of the effective normal stress clamping the fault (Guglielmi et al., 2014). When the fault is at rupture according to the Mohr-Coulomb failure concept, injection is maintained long enough to capture a significant amount of fault movement that can be used to characterize fault frictional and overall hydromechanical mechanism of reactivation.

Early injection cycles are meant to track early rupture initiation at the borehole wall but they may not represent well the fault rupture. Indeed, how a rupture initiates depends on borehole stress concentration with respect to the in-situ stresses, fluid viscosity, injection rate and the geometry of the borehole wall defects due to the geology and to the drilling (Lecampion et al., 2017). In addition, the injection pressure response to fracture initiation is often “hidden” by viscous effects associated to the borehole pressurization protocol and the fluid penetration in the created fracture. The early injection cycles are repeated until a clear breakdown pressure, which is the maximum pressure reached during the test, is reached and associated to pressurized flow forcing its way into the fault. After a few cycles of constant pressure steps, we switch to constant flow injection steps to propagate the rupture in the fault far enough from the injection borehole nearfield influence. One

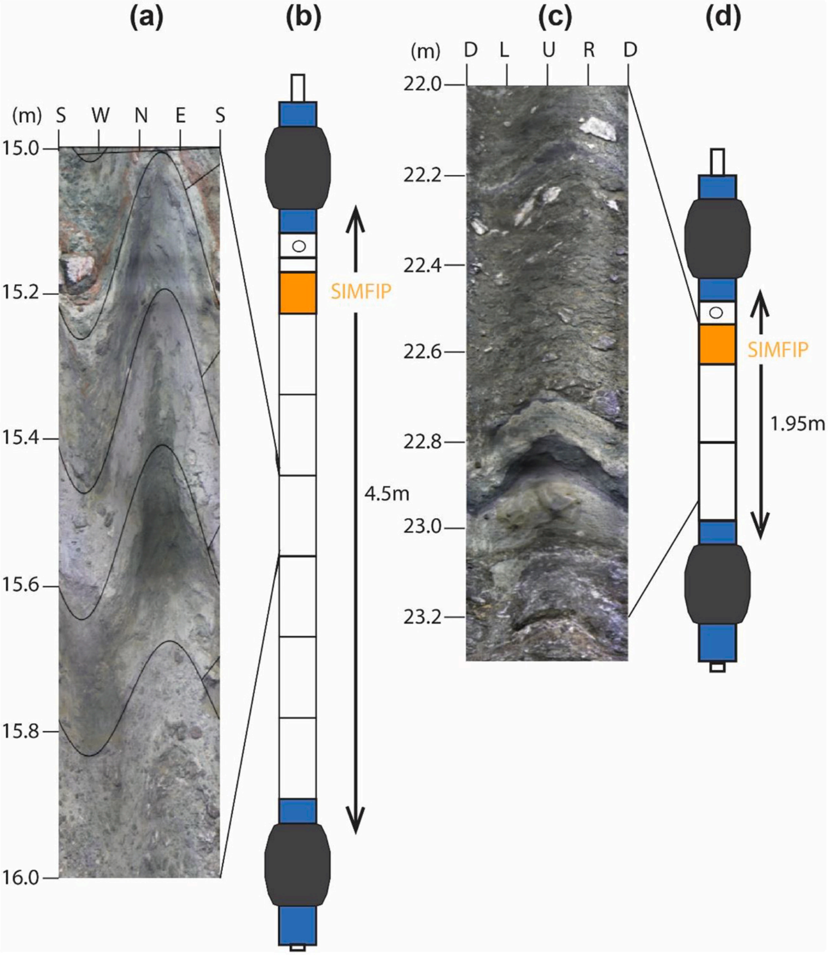

Fig. 3. SIMFIP probes deployed at Shionohira and Minakami-kita test sites and details of fault PSZ observed on borehole OPTV logs. Shinohira PSZ (a) and SIMFIP probe geometry (b); Minakami-kita PSZ (c) and SIMFIP probe Geometry (d).

way to control the size of the fault reactivation patch is to track the water pressure variation which is occurring when there is a hydraulic connection with a monitoring borehole set several meters away from the injection hole.

When the fault rupture is activated, the cage captures micrometer to millimeter three-dimensional displacements of the borehole that occur between the upper and the lower packers. The maximum displacement range of the SIMFIP is 0.7 and 3.5 mm in the axial and radial directions of the borehole, respectively, and the accuracy is $\pm 10 \times 10^{-6}$ m. A compass set on the probe provides the orientation of measurements with 0.1° accuracy. The stimulation pressure and injected flowrate are simultaneously measured during the test with precision of 10^4 Pa and 0.1 l/min, respectively downhole (point 4 in Fig. 2a) and at the ground surface. SIMFIP tests inform on:

- The fault activation pressure which is the pressure value when injection pressure starts dropping at constant injection rate;
- The mode of activation which is deduced from the orientation of the measured displacement versus the fault surface orientation;
- The irreversible displacement produced by the test which is the displacement value at the end of the test when borehole pressure has returned to its initial pre-test value.

2.2. *Fault surface rupture at Shionohira test site*

At the Shionohira site, the surface rupture related to the 04/11/2011 earthquake is characterized by a ~ 2 m high scarp with a dip direction/dip angle of 270°/74°. The fault scarp is cutting a small valley almost perpendicularly. The scarp bars the course of the small stream creating a pond (Fig. 4a). The fault eastern compartment is made of schists. The fault western compartment is made of gravels overlying sandstones. Outcrop observation revealed a principal shear zone (PSZ) with smooth surfaces and a thin fault gouge (Seshimo et al., 2015). In the eastern compartment, a fault fracture damage zone (FDZ) is affecting schist over several meters. In the western compartment, a meter thick FDZ is affecting the sandstones. Observation of polished slabs and thin sections sampled from the outcrop revealed normal faults in the western compartment's FDZ, and both normal (with a left-lateral component) and reverse faults in the eastern compartment.

Two fully cored vertical boreholes, 3 m horizontally spaced have been drilled about 6.0–6.8 m away from the fault scarp (Fig. 4b). Boreholes initiate in the fault western compartment made of intact sandstones overlaid by 7.0 m thick alluvial deposits (Fig. 4b). The sandstones contain conglomerate lenses and some bedding surfaces characterized by a variable 296°–350°/6°–60° orientation. The injection

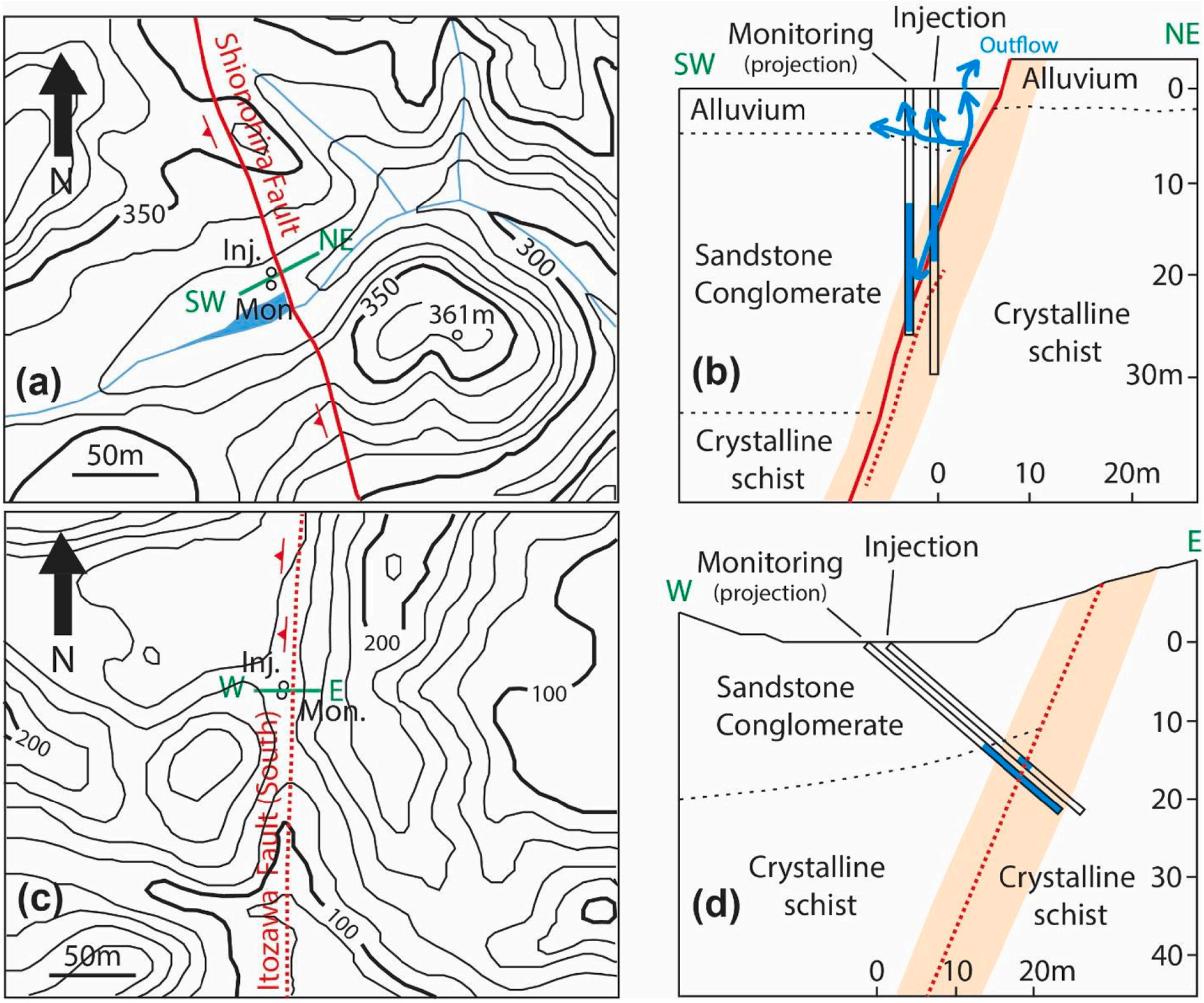

Fig. 4. Topography map, testing borehole locations and fault traces of the Shionohira (a) and Minakami-kita (c) sites. The geological profiles perpendicular to the Shionohira and Itozawa faults are illustrated in (b) and (d). Blue segments figure the borehole sealed intervals. Itozawa fault (south) is figured as red dashed line because it did not rupture during the earthquake. Approximate fault fracture damage zone (FDZ) thickness is figured in orange in (b) and (d). In Fig. 4d, the apparent fault offset corresponds roughly to the limit between the Sandstone and the schist (dashed sub-horizontal line) that is at about 10–20 m depth in the hanging wall, while the foot wall is all schist up to the land surface. (For interpretation of the references to colour in this figure legend, the reader is referred to the web version of this article.)

hole which is 30 m deep, is intersecting the fault zone at a depth of 14.4 m close to a complex tectono-sedimentary transition zone between conglomerates and crystalline schists (Fig. 4b). The PSZ has been intersected between 15.0 and 15.8 m depth (Fig. 3a). It is made of fine-grained material resulting from the comminution of schists during the fault movement. This material is affected by 249°/69–72° oriented slip surfaces. Below 15.8 m, the borehole is cross-cutting an older fault zone, that was not reactivated during the 2011 earthquake rupture. Down to about 24 m, the fault material looks almost similar, characterized by fine-to-relatively-coarse clasts with some apparent cements figured as white deposits. Caliper logs done a few days before starting the tests showed three significant borehole enlargements (washout), respectively between [14–15.8 m], [18–19 m] and [20–21 m] that resulted from the collapse of highly unconsolidated fine-grained shear layers. Below 24 m the schist looks much less brecciated. It corresponds to the fault fractured damaged zone down to the bottom of the borehole. The 28.6 m deep monitoring hole which is 3.1 m away from the injection hole displays the same geology. In that borehole, the activated PSZ is intersected between 15.94 and 16.6 m depth, and oriented 235°/76°–78°.

Three SIMFIP tests were completed in the injection borehole (Fig. 4b), respectively at [7–11.5 m] in the intact sandstone, at [12.8–17.3 m] across the activated PSZ and at [16.4–23.5 m] in the old inactive fault zone. Shear activation was only measured in the [12.8–17.3 m] interval set across the activated PSZ while mostly reversible re-opening of existing planes was detected in the other intervals, bedding planes in the sandstone and steeply dipping fractures in the old inactive fault zone. The amount of irreversible displacement was 10–100 times larger in the activated PSZ interval than in the other intervals while the activation pressure was equal to 5–7 times smaller (Table 1). These direct in situ observations show that the recently activated PSZ is the weakest zone intersected by the boreholes. In the following, we will focus on the analyses of fault movements triggered by injections in the [12.8–17.3 m] interval set across the activated PSZ (Fig. 3a and Table 1).

2.3. Minakami-kita test site

The Minakami-kita site is located across the inactive southern section of Itozawa fault (Itozawa fault (South) in Fig. 1). No surface rupture was observed after the 04/11/2011 earthquake (Figs. 1 and 4c). Two 50° inclined fully cored boreholes were drilled eastward from the surface with a 30 m length and a 3.7 m horizontal spacing (Fig. 4d, note that, in the following text, distance values correspond to the distance from the well head). The fault principal shear zone (PSZ) was detected at 20.40–23.10 m where a significant borehole enlargement corresponds to an ultrafine-grain shear zone with a dip direction/dip angle of 281–285°/67–80° (Fig. 3c). There is an apparent ~10–20 m normal fault offset (Fig. 4d). Indeed, the western fault compartment is characterized by a ~ 10–20 m thick pile of tertiary detritic and poorly cohesive sediments overlying crystalline schist, while the eastern compartment is only made of crystalline schist. The contact between tertiary sediments and schists is observed at 19.8 m in the injection borehole. From 18.7 m to the PSZ, the rock is strongly altered and affected by fracture planes parallel to the average fault direction. It corresponds to 1.5 m thick western fault damage zone. In the eastern compartment, the schist is fractured down to the bottom of the borehole at 30.0 m. It could correspond to a ~ 7 to 8 m thick eastern fault damage zone.

Four SIMFIP tests were completed in the injection borehole (Table 1), respectively at [17.85–19.8 m] mainly in the western fault damage zone including the contact with sedimentary rocks, [19.75–21.7 m] and [21.65–23.6 m] respectively across the top and bottom of the fault PSZ, and [23.29–25.24 m] in the eastern fault damage zone. Clear fault irreversible displacements have been observed in [19.75–21.7 m] and [21.65–23.6 m] intervals set across the fault PSZ. These two intervals display a roughly similar irreversible 270–321°/12–25° fault displacement, and 70–160 × 10^{-6} m of irreversible shear displacement (Table 1). The orientation of displacements is different. It is dipping South-East in [19.75–21.7 m] and North-West in [21.65–23.6 m] intervals. The reason is that the activated fault was outside the SIMFIP anchors/packers in [19.75–21.7 m], producing an apparent contraction on the SIMFIP. This was caused by a leak between the injection interval and the bottom hole zone that occurred through the formation. We can reasonably consider that the same shear zone located at 22.9 m and oriented 280–287/67–80 was activated with a significant borehole shear movement. No irreversible displacement was measured in the two fault damage zones [17.85–19.8] and [23.29–25.24] intervals, highlighting that no fault activation was triggered. The breakout pressures to activate fluid leakage in the fault were of 10.1–11 bars, respectively in [19.75–21.7 m] and [21.65–23.6 m] fault core intervals. In the [17.85–19.8 m] interval, pressure could not be increased because of the very high initial leakage in the formation. In the [23.29–25.24 m] interval, no leakage was observed even at a 17 bars maximum injection pressure.

Table 1
Testing results of SIMFIP at activated Shionohira-site and inactivated Minakami-kita site.

Site	Geology	Activated Structure and mechanism	Activation pressure (bar)	Amount of irreversible displacement (mm)
Shionohira Test depth (m) [7–11.5]	Intact sandstone/ conglomerate of the fault hanging wall	Mode 1 opening of 320–335°/ 2–24° bedding planes	2.1–2.25	0.15
Shionohira Test depth (m) [12.8–17.3]	Principal Shear Zone activated during the Fukushima ken Hamadori Earthquake of Mw 6.7	Dilatant shear slip on 249°/ 69–72° PSZ surface(s)	2.0–2.3	1.39
Shionohira Test depth (m) [16.4–23.5]	Ancient fault zone or Fault Damage Zone	Mode 1 opening of 280–290°/ 60–70° fractures or fault planes	>10	0.025
Minakami-kita Test distance from borehole head (m) [17.85–19.8]	Sedimentary breccia with heterogeneous clast size, and 5 open fractures.	None Large leakage into formation	None	None
Minakami-kita Test distance from borehole head (m) [19.75–21.7]	Fault core including the contact with sedimentary formation (19.8 m) and about 13 shear planes 271–300°/ 67–87°	Mode 2 activation of the 280–297/ 67–80 PSZ located at 22.9 m depth below the interval	11	0.15–0.16
Minakami-kita Test distance from borehole head (m) [21.65–23.6]	Fault core Including the 280–297/ 67–80 PSZ. This zone is a 0.1 m thick layer of fine grain material.	Mode 2 activation of the 280–297/ 67–80 PSZ located at 22.9 m depth	10.1	0.7–0.8
Minakami-kita Test distance from borehole head (m) [23.29–25.24]	Cohesive fractured schist with a lot of silica veins and 13 fractures.	None No Leakage observed	None	None

The activation modes, activation pressures and irreversible displacements measured at the end of each test at different testing intervals are listed.

These direct in situ observations show that the [21.65–23.6 m] interval, including the PSZ, is the weakest zone intersected by the boreholes. In the following, we will focus on fault movements triggered by injections in this interval (Table 1).

3. Field measurements during the hydraulic tests

3.1. Selected tests and Injection sequence

In this chapter, we compare fault movements triggered by injections conducted at both the Shionohira and the Minakami-kita sites using tests done in the following intervals (Table 1):

- the [12.8–17.3 m] interval set across the PSZ of the Shionohira fault that was activated by the Fukushima-ken Hamadori Earthquake (Shinohira site);
- the [21.65–23.6 m] interval set across the PSZ of the inactive southern section of Itozawa fault (Minakami-kita site).

Both intervals were recognized as the weakest zones intersected by the injection boreholes. They both include the principal shear zone (PSZ) of the fault.

In both sites, the injection sequence is the same. It is characterized by two contrasted testing periods (Fig. 5). Taking the example of the Shionohira site test sequence (Fig. 5a), we first injected a small water volume of 6.4 l using a manual pump in order to initiate the fault reactivation at the borehole wall during the [11:25–12:12] period. Each manual pump stroke was 1-s-long and corresponds to 15 ml of injected water. Pressure was increased step-by-step by increments of 0.5 bar. After each pressure step, the pumping was stopped for about 2 min.

Second, during the [13:21–15:06] period, a large water volume of 1.53 m^3 was injected with an engine pump in order to extend the size of the rupture patch in the activated fault, significantly away from the injection borehole influence. The flow rate was increased step-by-step from 7.6–50.1 l/min, at each step the flowrate being hold constant for ~1.5 min.

3.2. Shinohira [12.8–17.3 m] interval across the activated PSZ

During the [11:25–12:12] period, rupture initiates between 2.6 and 3.8 bars, and is associated to a pressure drop (that occurs after the pumping was stopped at the given pressures, Fig. 5a).

During the [13:21–15:06] period, the ruptured patch produced by the [11:25–12:12] period was hydraulically re-opened during the first applied flow step of 7.6 l/min (Fig. 5a and 6a). In Fig. 6a, chamber pressure reached 4.76 bars after 24 s of injection, before decreasing to an almost constant value of 3.8 bars towards the end of this initial 7.6 l/min step (Fig. 6a, point 1 at 2 min and 4 s). The onset of the pressure decrease corresponds to the fault hydraulic opening pressure (FOP in Fig. 6a). Then, pressure stayed roughly constant at about 3.8 bars during the following flow step increases from 7.6 to 50.1 l/min (Fig. 6a). In details, there is a pressure increase occurring at each flow rate increase. Then, after pumping is stopped, there is a pressure decrease to ~3.8 bars. This is happening at each flow step from 7.6 up to 50.1 l/min. When flow rate is stepped down at 33 min and 39 s (point 5 in Fig. 6a), there is a corresponding pressure step down, back to the initial interval pressure. Fig. 6b and c show that both the monitoring borehole located 3 m away and the pressure in the hanging wall sandstones (which is measured in the injection well above the upper packer) reach a constant value after 6 min and 39 s and 8 min and 22 s of injection, respectively (Fig. 6 points 2 and 3). This means that at this time water is outflowing at both borehole heads. Meanwhile, a very small pressure variation is observed below the sealed section in the injection well, occurring during the first steps and related to the lower packer mechanical response to pressurization in the interval (Fig. 6b). Finally, a 1.1 l/min outflow is observed at the ground surface (outflow was estimated using a 10 l bucket), 4 m away from the injection well and after 22 min and 53 s of injection (Fig. 6 point 4 and Fig. 4b for location). These observations display the following information:

- Leakage occurred in the permeable sandstones,
- No leakage was observed in the metamorphic footwall,

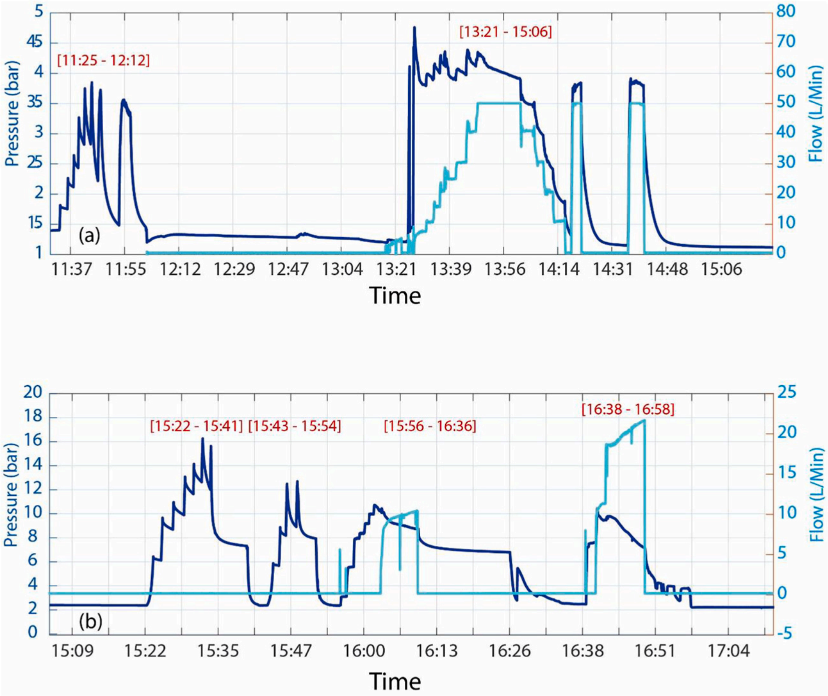

Fig. 5. (a) Test sequence at the Shinohira site; (b) Test sequence at the Minakami-kita site.

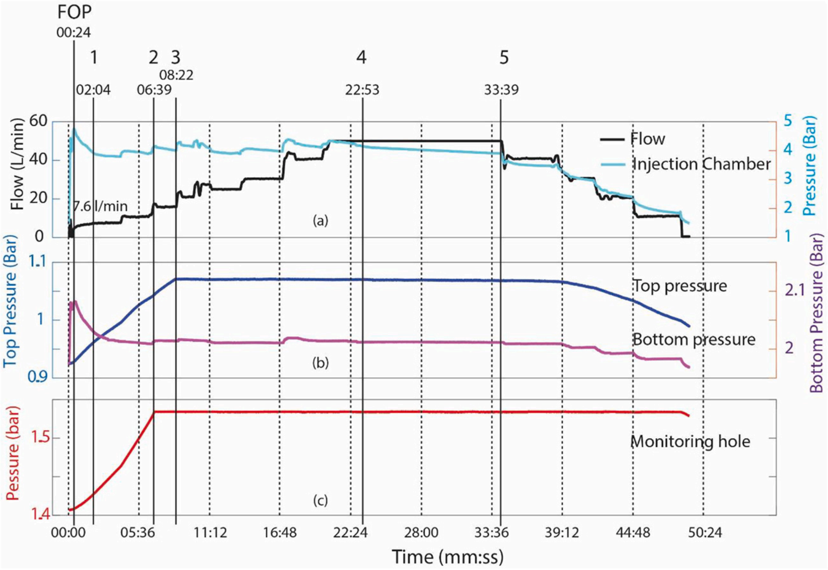

Fig. 6. Shinohira [13:21–15:06] step-rate test (a) Imposed flowrate and measured chamber pressure in the injection borehole; (b) Pressure variation in the injection borehole respectively above the sealed interval in the fault western compartment sandstones (Top pressure) and below the sealed section in the metamorphic rock (bottom pressure); (c) Pressure variation at the monitoring hole (Fig. 4 for location).

- The fault pressurized patch radius was of ~10–20 m (if we consider the distance between the injection interval and the outflow at land surface as a rough estimation of the patch radius, Fig. 4b),
- Ground surface acted as a hydrogeological constant pressure boundary during the test.

Fig. 7a shows that the three-dimensional borehole displacements variations during the [13:21–15:06] period are characterized by three successive phases:

- Initial fracture hydraulic re-opening phase (black segment in Fig. 7). The fracture reopening phase corresponds to the first 2 min and 4 s of injection including the FOP and "ending" at point 1 in Fig. 6a. When applying the first step of 7.6 l/min constant flowrate during this period, a horizontal EW displacement is first observed before FOP (Fig. 7b). This initial displacement is related to the borehole wall elastic response to pressurization before leakage occurs into the fault. At FOP and until point 1, a vertical displacement initiates (see FOP-to-point 1 segment in Fig. 7b) in addition to a re-orientation of the horizontal displacement parallel to the fault's strike (Fig. 7c). As soon as the vertical displacement initiates, there is a pressure decay (see FOP to point 1 segment in Fig. 6a) showing that the fault is hydraulically opening. Synchronously, displacement progressive re-orientation parallel to the fault's strike highlights that the fault starts shearing (Fig. 7c).
- Propagation of fault rupture (red segment in Fig. 7). The fault rupture propagation corresponds to the period from point 1 to the onset of the pressure step down at point 5 in Fig. 6. When flowrate is increased step-by-step, displacement orientates almost parallel to the fault's strike (Fig. 7c), corresponding to a left-lateral strike slip movement with a reverse component (meaning that the fault western compartment is moving upwards and southwards along the fault surface compared to the fault eastern compartment which is moving downwards and northwards, Fig. 7). Fig. 7d shows the stereographic projection of the displacement vector $\overrightarrow{15}$ that is calculated between the displacements measured at points 1 and 5 bounding the rupture propagation period (red segment in Fig. 7). It results that rupture propagation away from the borehole influence is characterized by a borehole displacement dip direction/dip angle of 320°/15°. This vector is consistent with the opening of the fault, the two walls of the fault PSZ moving away from each other along a direction perpendicular to the fault PSZ, associated to the reverse shearing of the fault, the western compartment moving up along the dip of the 249°/69–72° PSZ straddled by the probe in the injection interval (Fig. 7d).
- Fault closing during pressure step-down (green segment in the Fig. 7). When flowrate is step-decreased (after point 5 in Fig. 6a), there is a vertical contraction of the borehole with a horizontal component oriented as the initial pre-FOP displacement. The residual displacement observed at the end of the test matches with the inelastic fault slip period that occurred during rupture propagation (compare for example the distance between the beginning and the end of the test, and the length of the red segment in the Fig. 7c).

In Fig. 8, we have isolated the fault tangential displacement periods that occur during the rupture propagation phase (red segment in Fig. 7). In order to avoid the influence of artificial pressure variations when the flowrate is varied from one constant step to the other, we only pick the fault shear and normal opening variations during the constant flowrate periods (colored segments in Fig. 8). There is no clear relationship between fault movements and the injection flowrate. The shear and normal opening during the first flow step display a significantly different shear displacement amplitude and normal opening compared to the following steps (Fig. 8b, c). Since it corresponds to the early fault rupture propagation associated to the reorientation of the displacements parallel to the fault strike, such a difference is interpreted as the influence of some borehole nearfield heterogeneity affecting the rupture patch which is of limited extension at this time of the test. During the following steps, while the patch is extending several meters beyond the influence of the borehole, fault shear roughly displays about the same range of variations. There is a non-linear shear displacement increase with time that is almost symmetrical to the synchronous pressure decay. Except steps 7.6 and 30.6 l/min, this is associated to a normal opening. Thus, observations show that when the rupture patch extension is large enough within the fault PSZ, shear induces fault dilation and associated decrease in pressure at constant injection flowrate.

3.3. *Minakami-kita [21.65–23.6 m] interval across the inactive PFZ*

As mentioned in chapter 3.1, the test sequence is similar to the one conducted at the Shionohira site in the way that we first start with

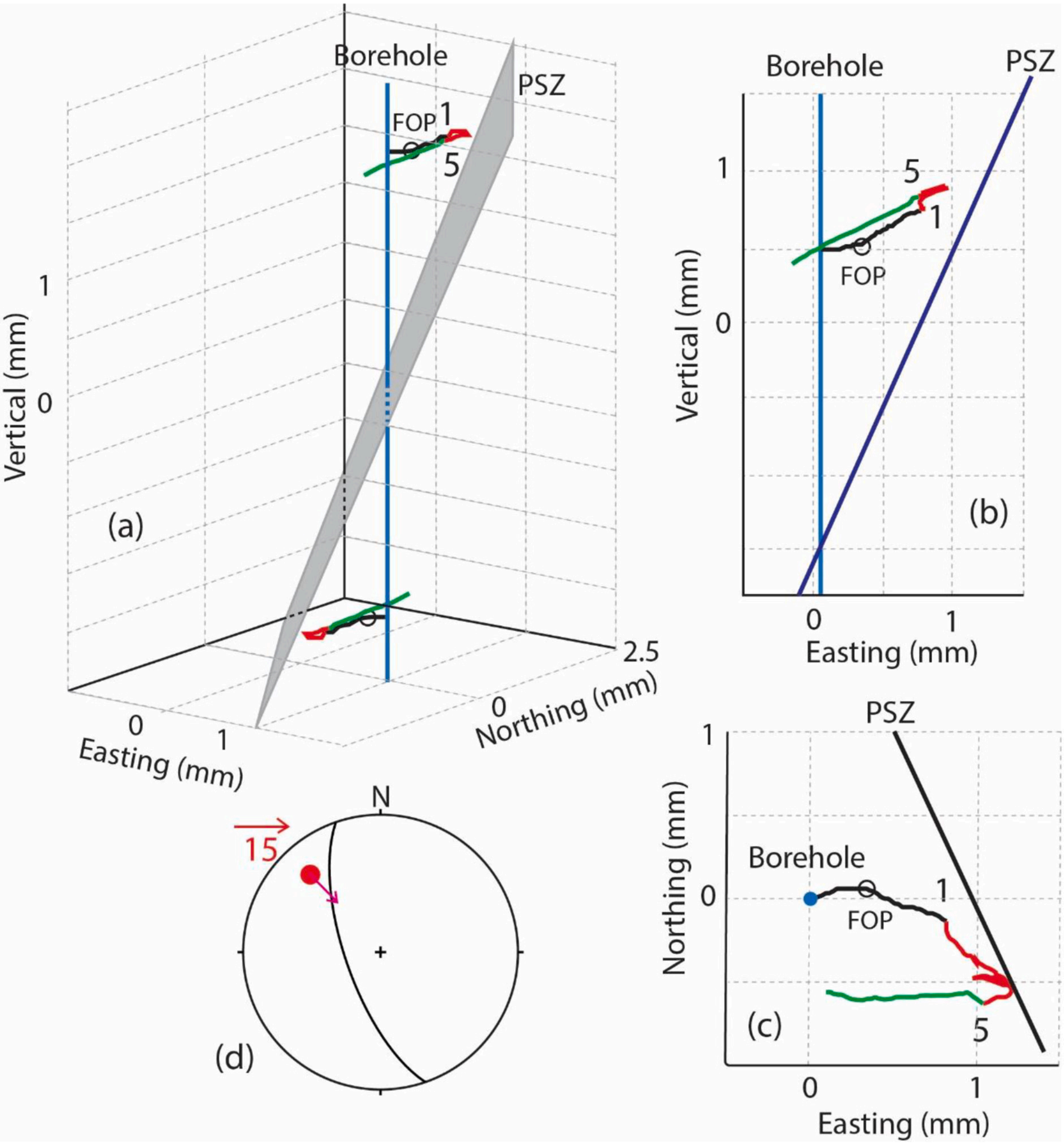

Fig. 7. Borehole displacements during Shinohira [13:21–15:06] test (a) Three-dimensional view; (b) Vertical plane view perpendicular to the fault PSZ strike; (c) Horizontal plane view; (d) Lower hemisphere stereographic projection of the PSZ trace and of vector $\overrightarrow{15}$ corresponding to displacement between points 1 and 5. Curves' colors are used in the text to describe the fault reopening (black), the propagation of fault rupture (red) and the fault closing (green). FOP is the Fault Opening Pressure. (For interpretation of the references to colour in this figure legend, the reader is referred to the web version of this article.)

manual pump injections and then conduct engine pump injections. The idea is to first initiate rupture and then to propagate it. The test sequence is characterized by four injection periods (Fig. 5b). Compared to tests performed at the Shionohira site, all injection periods were pressure-controlled. It means that the increase in the injection chamber's pressure was conducted by steps of fixed constant pressure until fault activation. At fault activation pressure, the mechanical opening of the fault caused an un-controlled pressure drop (Fig. 5b, seen on all periods) and a sudden increase of the injection flowrate from a null value (Fig. 5b, seen on [15:56–16:36] and [16:38–16:58] periods which were the only cycles when flowrate was monitored). During [15:22–15:41] and [15:43–15:54] periods, pressure was increased by injecting small water volumes with a manual pump, respectively of 2.25 and 1.5 l. No pressure variation was observed above or below the injection interval, and at the monitoring borehole. We switched to an engine pump in order to inject larger volumes in [15:56–16:36] and [16:38–16:58] periods, in order to extend the rupture in the fault away from the borehole influence. Then, a pressure increase marked the hydraulic connection with the monitoring hole. Given the distance between the two boreholes, it allows estimating that the activated patch had hydraulically extended of at least 3 m away from the injection hole. Injected volumes during [15:56–16:36] and [16:38–16:58] periods were of 56.8 and 213.6 l, respectively. The breakdown pressure decreases from 16.3 to 10.5 bars from period [15:22–15:41] to [16:38–16:58], respectively. It highlights that it was easier and easier to open and activate the fault while repeating the pressure cycles.

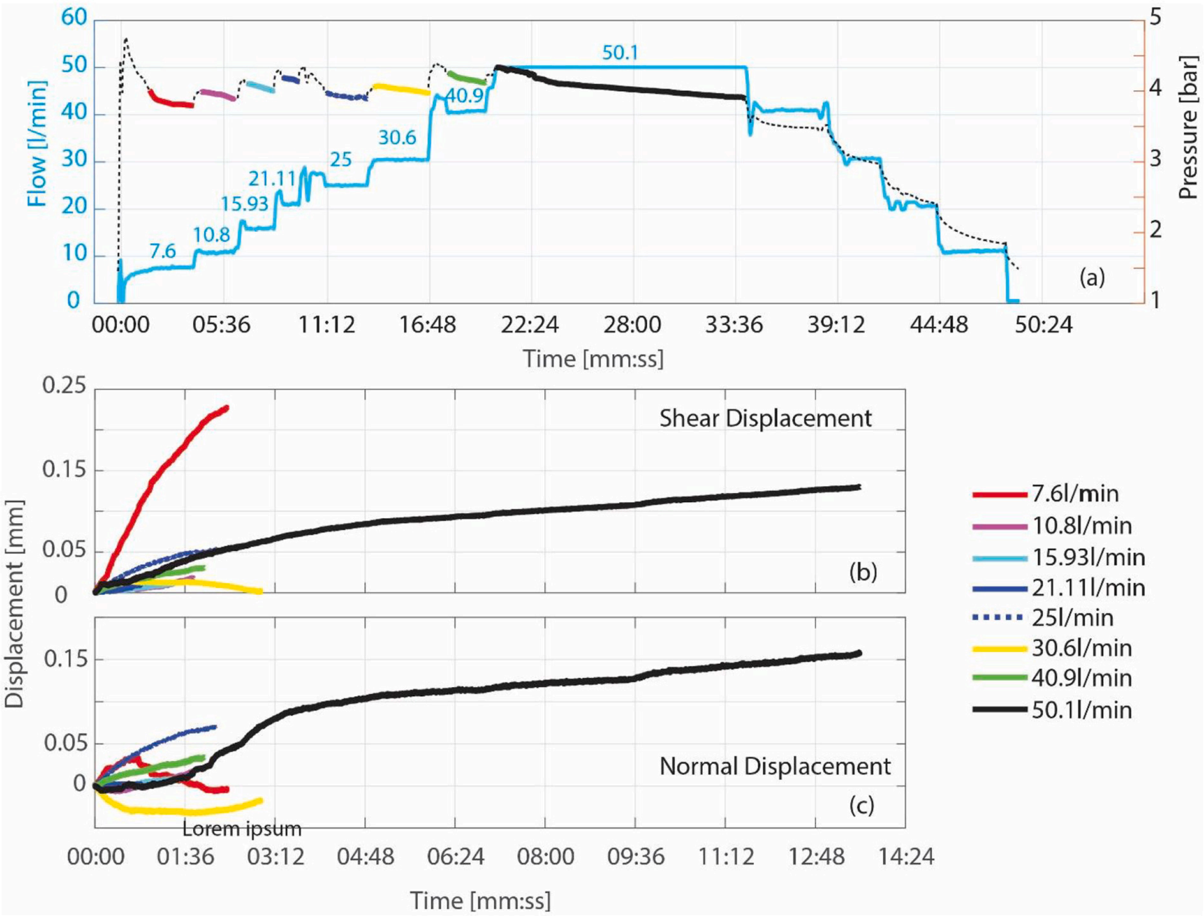

Fig. 8. Shear and Normal Displacement of Shinohira PSZ during the [13:21–15:06] test (a) Colored segments showing time periods selected on the pressure curve to plot the fault displacements outside the influence of the artificial flow step increases; (b) Fault shear displacement versus time; (c) Fault normal displacement versus time (we selected the 249°/69° PSZ surface to calculate the shear and normal displacement from the three-dimensional borehole displacements).

Fig. 9a–d show that, during the [15:22–15:41] period, fracture activation initiates with a 270°/30° borehole displacement, corresponding to an opening of the fault with a downward displacement of the fault western compartment parallel to the borehole axis direction (cyan segment in Fig. 9a–d). Then, there is a significant rotation of the displacement (magenta period in Fig. 9a–d). Fig. 9d is showing the 220°/10° dip direction/dip angle vector calculated between displacements at the onset and at the end of the magenta segment. This displacement is consistent with the opening and downward left-lateral shearing of the 285°/80° PSZ straddled by the probe in the injection interval. When pressure is decreased, borehole displacement trend is roughly the reverse of the initial one (compare black segment orientation with cyan segment in Fig. 9a–c), but with a larger magnitude. At the end of the [15:22–15:41] period, there is a ~ 0.2 mm residual displacement showing that some irreversible fault activation occurred. This irreversible displacement apparently mainly relates to the left lateral shear period (magenta in Fig. 8a–c). Fig. 9e–h show, that during the [15:56–16:36] period, the left lateral fault shear is more pronounced. Here, the displacement vector in Fig. 9h is calculated between the onset of the cyan period and the end of the red period. The 223°/14° dip direction/dip angle vector corresponds to a similar fault movement as the one deduced from the [15:22–15:41] period (compare Fig. 9d and h). Nevertheless, during the shut-in and the interval pressure bleed-off period (respectively magenta and black segments in Fig. 9e–g), it appears that most of this displacement is reversed. At the end of the [15:56–16:36] period, the residual displacement is ~0.2 mm, in the same range as observed after cycle 1. Thus, propagation of rupture from the [15:22–15:41] to the [15:56–16:36] period is characterized by fault opening and shearing with a cumulated irreversible displacement of ~0.4 mm and a reversible displacement of ~0.5 to 0.6 mm mainly observed in periods [15:22–15:41, 15:56–16:36]. Most of the last [16:38–16:58] period induced reversible displacement.

Fig. 10a–c shows that, during the [15:22–15:41] period, rupture initiates during the maximum pressure increase (cyan segment in Fig. 10a) with about the same amount of shear and normal opening on the fault. This is thus corresponding to a highly dilatant event. Same thing occurs when pressure is artificially increased again, but this second time there is more shearing than fault normal opening (magenta segment in Fig. 10a). The red segment that is observed between the two pressure activation events (cyan and magenta in Fig. 10a) shows shear increasing while there is a slight fault normal closing. This might be explained by pressure diffusing into the activated zone that favors fault shear and associated dilation. Dilation increases fault leakage and pressure decrease since no flow is injected in the interval to maintain the pressure constant during this period of time. The apparent overclosure and shear at the end of the period is related to the complex three-dimensional movement of the borehole relative to the fault as shown in Fig. 9a–c. During the [15:56–16:36] period (Fig. 10d–f), there is a highly non-linear fault re-opening and shear characterized by cyan and red segments. First, fault re-opens and re-shears at high pressure of 10.7 bar but with no significant variation in flowrate (cyan segment). Then, rupture growth initiates after a new attempt to artificially increase pressure (red segment), with an increase in both opening and shear. This is associated to a significant increase in flowrate. When the injection chamber is shut-in (magenta segment in Fig. 10d), there is a slow negative shear and normal closing of the fault. This trend continues even

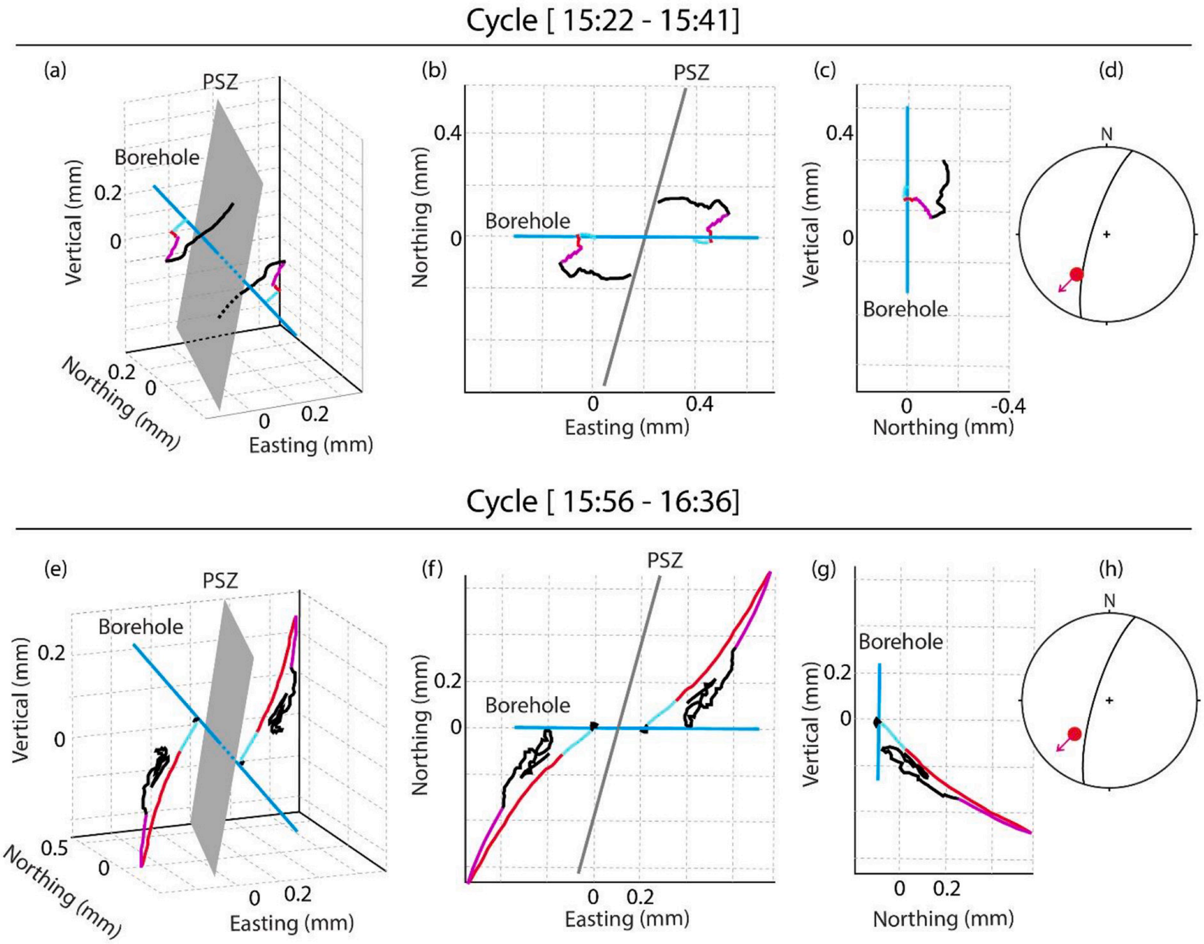

Fig. 9. Minakami-kita's borehole displacements spatial variations during pressure cycles [15:22–15:41] and [15:56–16:36]. Pressure cycle [15:22–15:41] (a) three-dimensional displacement, (b) Horizontal displacement, (c) Vertical-Northern displacements and (d) Stereographic projection of the fault displacement vector (calculated between displacement at the beginning and at the end of the red segment). Pressure cycle [15:56–16:36] (e) three-dimensional displacement, (f) Horizontal displacements, (g) Vertical-Northern displacements and (h) Stereographic projection of the fault displacement vector (calculated between displacement at the beginning of the blue period and at the end of the red period). Colored segments show different time periods occurring during the tests (see Fig. 10 for the time periods). (For interpretation of the references to colour in this figure legend, the reader is referred to the web version of this article.)

after the chamber bleed-off. At bleed-off, a transient pressure increase is observed associated to mainly reversible shear and normal displacement of the fault. This transient may correspond to flow back from the activated patch into the borehole (although this could not be measured during the test), indirectly informing that a relatively little leakage from the ruptured patch into the surrounding rock may have occurred.

4. Three-dimensional numerical analyses of faults hydromechanical activation

4.1. Model set-up

The 3DEC distinct element code (Itasca Consulting Group, 2016) is used to represent a fault in a three-dimensional model of about 20 × 20 × 20 m (Fig. 11). Fault orientation is 249°/69° and 285°/80° at Shinohira and Minakami-kita sites, respectively (Fig. 11a and d). At Shinohira, the fault scarp affecting the topography after the 04/11/2011 earthquake is represented.

The fault is modeled as a thin planar interface separating two compartments represented as two elastically deformable and hydraulically permeable blocks that are free to move, rotate and separate relative to one another. In addition, water leakage between the fault plane and the blocks is allowed. Flow in the blocks follows the Darcy law. The fault plane is divided into 0.2 to 0.6 m mesh elements that represents contacts between the two deformable blocks. At each time step, the laws of motion and constitutive equations are jointly applied to calculate normal and shear forces at each contact, which then are used in the calculation of the block motion using a time-domain dynamic algorithm. The fault constitutive model is the generalization of the Coulomb friction law. We use two Mohr-Coulomb models, a constant friction and a linear slip-weakening friction model. The linear slip-weakening law assumes that the friction coefficient (μ) depends on the amount of slip (D) and decays linearly from a peak static value (μ_s) to a residual dynamic value (μ_d) over a critical slip distance (δ_c, and Eq. (1)):

$$\mu = \begin{cases} \mu_s - (\mu_s - \mu_d)\dfrac{D}{\delta_c} \quad D < \delta_c \quad \mu_d \quad D > \delta_c \end{cases} \tag{1}$$

In addition, following the concept developed in Guglielmi et al. (2020), our model allows for fluid flow only through the ruptured (either in shear or tension) parts of the predefined fault plane. This is justified by no observed injection flow when a low injection pressure was applied in the test zones, highlighting an initial fault aperture close to zero (Fig. 5). Thus, the fluid has to force its way into ruptured area of the fault. In the model, the injection is applied in one contact element in the middle of the fault plane. Outside of this element, contacts must rupture for the fluid flow to occur within the fault plane. When a plane element is ruptured, fluid flow is calculated using the modified cubic law (Witherspoon et al., 1980), where the hydraulic aperture is dependent

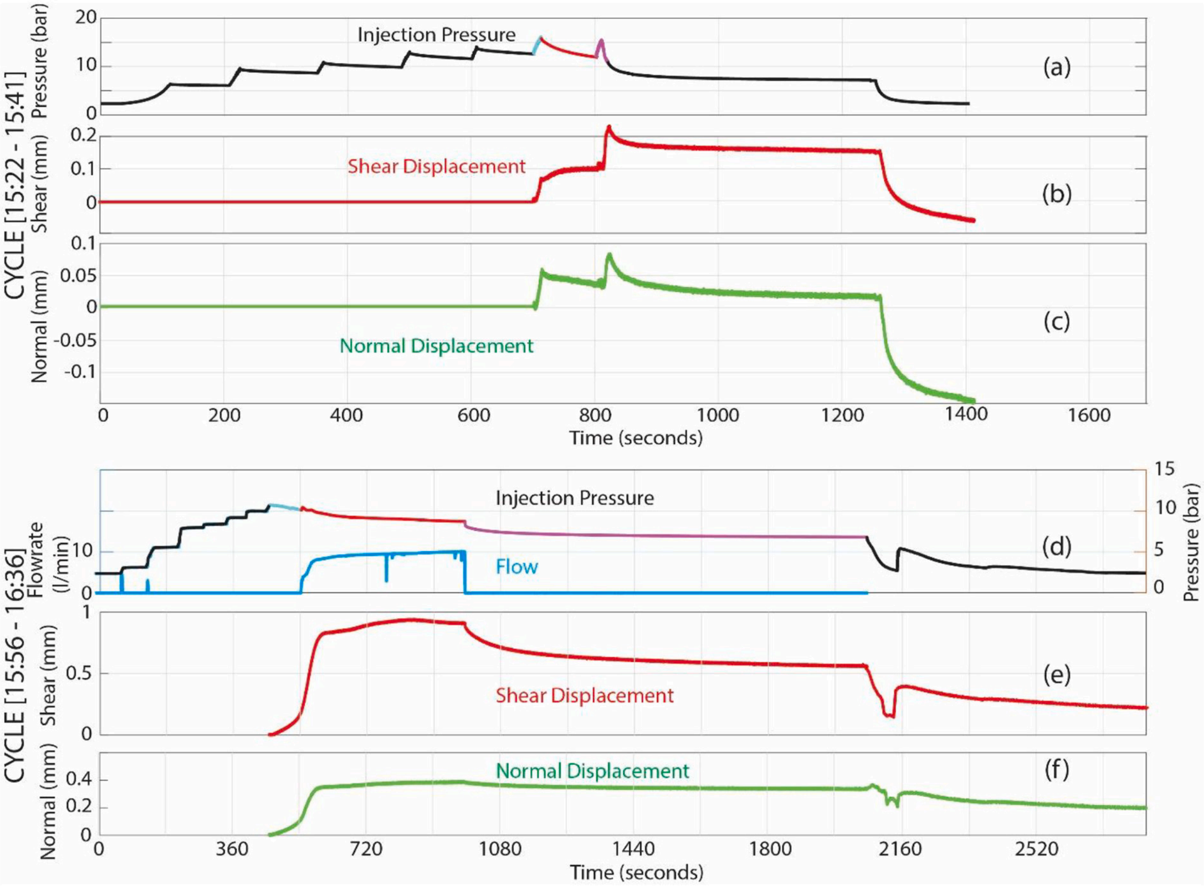

Fig. 10. Minakami-kita's PFZ shear and normal displacements temporal variations during pressure cycles [15:22–15:41, 15:56–16:36]. Cycle [15:22–15:41], (a) Injection pressure, (b) Shear displacements and (c) Normal displacement. Cycle [15:56–16:36], (d) Injection pressure, (e) Shear displacements and (f) Normal displacement. Colored segments show different time periods occurring during the tests (see Fig. 9 for the spatial variations of displacements during these periods of time).

on the fracture deformation (opening and shear-induced dilation) to account for the stress-dependent fracture hydraulic conductivity (Detournay, 1980).

The two models were initially consolidated under gravity force, with null velocity boundaries applied perpendicularly on the four vertical sides and on the bottom side of the model. The top side of the model was set free to move because it corresponds to the topographic surface. In the Shionohira model, the upper 5 m of the south side were also set free to move in order to represent the influence of the nearby valley on model stresses (Fig. 4a). Nevertheless, both models oversimplify the local topography which might play complex effects on the stress distribution around the faults. In both models, a groundwater table was set at 3.5 and 6.5 m depths in Shionohira and in Minakami-kita, respectively. Hydraulic and mechanical properties found in the bibliography (Kuwahara et al., 1991) were assigned to faults and surrounding rocks, and adjusted after matching the calculated fault fluid pressure and mechanical displacements to the field measured ones (Table 2).

With this numerical modeling approach, we do not attempt to make an exact match of simulated and experimental data. The observed discrepancy is related to the simple homogeneous properties assigned to the fault and to the intact rock, the schematic fault zone geometry, and the simplified overall site hydrogeological context (the topographic surface is poorly figured as an example). We rather try to obtain a reasonable agreement to the general evolution of pressure and displacement data in order to explore the mechanisms of activation and inactivation of the two explored fault segments. Consequently, we focus on modeling the key test periods described in Section 3, the second [13:21–15:06] period of Shionohira test sequence and the [15:22–15:41, 15:56–16:36] periods of Minakami test sequence. All model cases are summarized in Table 2. In the Shionohira case, our baseline model 1 (i.e the «best» match to the experimental data, Table 2) is considering that a high permeability of the sandstone conglomerates controls leakage in the fault hanging-wall, and influences fault displacements and pore pressure. We then conduct models 2, 3 and 4 where we respectively vary the hanging-wall permeability, the fault friction and stiffness (Table 2). Finally, we consider the possibility for the fault friction to decrease with fault slip (slip-weakening model 5). In the Minakami case, we use the [15:22–15:41] period to match a best fit case (model 1, Table 2) for fracture initiation and we conduct a sensitivity study by varying fault friction, fault cohesion and the normal stress applied on the fault (models 2-3-4, Table 2). Then we use model 1 properties to analyze the [15:56–16:36] period where our stimulated fault volume grows away from the injection borehole. We explore what may explain the differences with the first activation period by considering a lower friction of the fault (model 5), a more complex fault structure (model 6) and a complex interaction between a newly formed fluid driven fracture and the natural fault (model 7).

4.2. *Estimations of the in-situ stress tensor*

In Fig. 11 and Table 3, we compare the state of stress calculated on the fault planes after the hydromechanical consolidation of the forward model under gravity, using the rock properties listed in Table 2, with an inverse approach based on a fault dislocation analysis during fluid injection (Kakurina et al., 2019, 2020). First, we consider the orientation of the slip component of the measured SIMFIP displacement vector

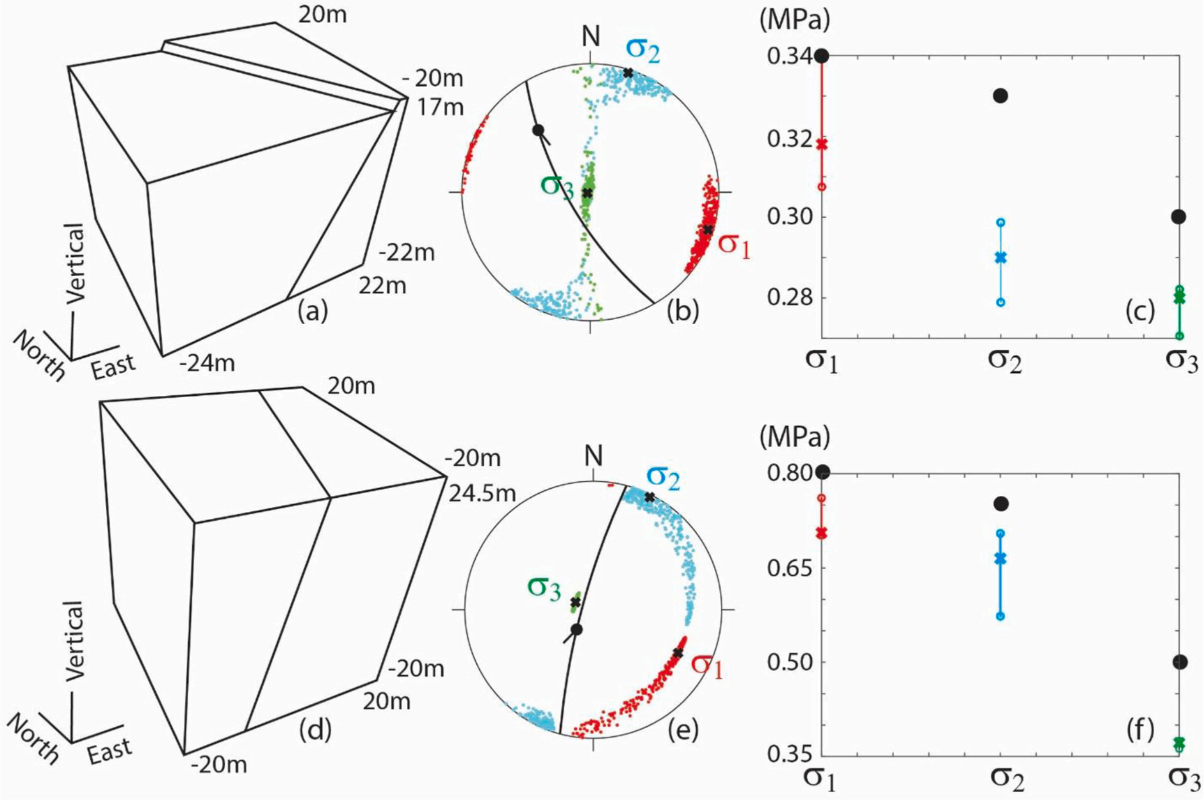

Fig. 11. Stress estimations. Numerical model settings of (a) Shinohira and (d) Minakami-kita sites. Orientation of the principal stresses projected in a lower hemisphere stereogram for Shionohira (b) and Minakami-kita (e). Black cross dots are the median principal stresses. Small colored dots figure all possible solutions (Red colour corresponds to σ_1, green to σ_3 and blue to σ_2). Principal stress magnitudes estimated at Shionohira (c) and at Minakami-kita (f). Colored crosses show the median principal stress magnitudes deduced from the inverse approach. Black circular dots show principal stress magnitudes calculated by the forward numerical model. (For interpretation of the references to colour in this figure legend, the reader is referred to the web version of this article.)

Table 2
Hydromechanical properties of numerical models for the two test sites.

	Shionohira					Minakami							Units
Model	1	2	3	4	5	1	2	3	4	5	6	7	
Properties													
Bulk modulus of hanging wall *(K)*	15					19							GPa
Shear modulus of hanging wall *(G)*	11.25					14.25							GPa
Hanging wall density *(ρ_r)*	1900					2800							kg/m^3
Hanging wall permeability *(Kh)*	10^{-10}	10^{-18}	10^{-10}	10^{-10}	10^{-10}	10^{-18}							m^2
Hanging wall porosity *(m)*	0.5					0.05							
Bulk modulus of foot wall *(K)*	19					19							GPa
Shear modulus of foot wall *(G)*	14.25					14.25							GPa
Foot wall density *(ρ_r)*	2800					2800							kg/m^3
Foot wall permeability *(Kh)*	10^{-18}	10^{-18}				10^{-18}							m^2
Foot wall porosity *(m)*	0.05					0.05							
Fault elastic stiffness *(k_n, k_s)*	12, 12			18,18		10, 10							GPa/m
Static Friction	14		10			19			18	14			(°)
Peak Friction					18								(°)
Residual Friction					10								(°)
Critical Slip Distance					10^{-6}								(m)
Cohesion/Tensile strength	(0,0)					(0.4,0.2)		(0,0)					(MPa)
Initial hydraulic aperture *(a_{ho})*	10					10							µm
Dilation angle *(ψ)*	5					5							Degree
Fluid Bulk modulus (K_w)													
Fluid density (ρ_f)	2					2							GPa
Fluid viscosity (μ_f)	1000					1000							kg/m^3
	0.001					0.001							Pa.s

Models 2, 6 and 7 of the Minakami-kita site have the same hydromechanical properties as the reference model 1. The difference is that larger magnitudes stresses are applied at the model 2 boundaries, and that models 6 and 7 include several fracture planes.

Table 3
Summary of stress estimations.

Case	Depth	σ_1		σ_2		σ_3		σ_v	Activated fault		Slip	
	m	dd/d	MPa	dd/d	MPa	dd/d	MPa	MPa	dd	d	dd/d	sense
Shionohira	15	108/2	0.32	18/2	0.29	254/87	0.28	0.3	249	69	320/−15	TF
Minakami	15.6	117/17	0.7	27/1	0.68	293/73	0.38	0.4	285	80	220/10	NF
Model Shionohira	15	1/12	0.34	270/5	0.33	157/78	0.30	Adjusted To depth	249	69		
Model Minakami	16	90/0	0.8	180/0	0.75	298/90	0.5	Adjusted To depth	285	80		

The two upper rows are the inverse analyses and the two lower rows are the forward numerical analyses (dd – dip direction; d – dip; TF – Thrust Fault; NF – Normal Fault).

(Figs. 7d, 9d–h and Table 3). A slip direction is calculated on the fault plane considering the hypothesis that slip is consistent with the direction of the resolved shear stress on the plane (Wallace, 1951; Bott, 1959). We search for all possible reduced stress tensor solutions that fit the measured slip. The slip direction is calculated using the reduced stress tensor defined over a computational mesh of 59,400 grid points with 300 directions of σ_3 with nearly equal intervals, 18 directions of σ_1 for each σ_3 with an interval of 10°, and 11 variations of stress ratio R with an increment of 0.1 for each combination of σ_1 and σ_3, following the approach developed by Yamaji (2003). To maximize the fit of the assumed stresses from the grid to the observed data, we use the objective function recommended by Angelier (1979) which depends on both the direction and sense of the fault motion. To reduce the number of possible solutions, we keep the reduced stress tensors with a maximum misfit angle between the calculated and measured slip of 5°. Second, we estimate the absolute principal stress magnitudes σ_1, σ_2, σ_3 by solving the system of equations below:

$$\begin{cases} R = (\sigma_2 - \sigma_3)/(\sigma_1 - \sigma_3), \\ \sigma_n = l_1^2\sigma_1 + m_1^2\sigma_2 + n_1^2\sigma_3 \ , \\ \sigma_v = l_2^2\sigma_1 + m_2^2\sigma_2 + n_2^2\sigma_3 \end{cases} \tag{2}$$

where l_1, m_1, n_1 and l_2, m_2, n_2 are the direction cosines of the normal and vertical components of the fracture with respect to the principal stress axes. R is the reduced stress tensor. σ_v is the vertical stress. σ_n is the fracture normal stress. For the Shinohira and Minakami tests, the vertical stress was estimated by the weight of the overburden considering a 1900 and 2800 kg/m^3 density respectively (Table 2). In the Shionohira inversion, we approximate σ_n to the injection pressure of 3.8 bar corresponding to the average value of the 2.8 to 4.8 bar pressures measured at fault opening during the [11:25–12:12] injection cycle (Fig. 5a). Since some slip may have initiated as well as fault opening, this is certainly a rough estimation of σ_n. In the Minakami inversion, we approximate σ_n to the pressure of 6.8 bars measured at the end of the [15:56–16:36] cycle shut-in period (Fig. 5b). We finally get several possible reduced stress tensor solutions (colored dots in Fig. 11b–e), with the median stress tensor solution having about the same orientation in both sites (black crosses in Fig. 11b–e). It is characterized by a sub-vertical σ_3 certainly explained by the shallowness of the tests. σ_1 and σ_2 respectively are sub-horizontal, and respectively EW and NS oriented. These directions have no clear correlation with the ones deduced from the focal mechanism of the Fukushima-Hamadori earthquake at depth (Yoshida et al., 2015), and we know no shallow stress measurement performed in the area after the earthquake. In addition, the magnitudes of all three principal stresses are very close to each other, highlighting a relatively isotropic in-situ state of stress. Black circular dots in Fig. 11c–f and Table 3 show that the stress tensor magnitudes derived from the 3DEC model match reasonably well with the tensor estimated from the inversion of the fault displacement. We thus estimate that the fault reactivations observed in the field were performed at such a shallow depth that activation modes are much more related to fault properties and orientation than to the in-situ stress tensor in such tests. This comparative approach also allows us "validating" the boundary conditions applied in the numerical model that restitutes stress magnitudes and orientation in reasonable accordance with the inverse approach.

We then applied the hydraulic injection protocol conducted in the field, respectively the flow-controlled engine pump injection during the [13:21–15:06] period at Shionohira and the pressure-controlled [15:22–15:41, 15:56–16:36] injection periods at Minakami-kita (Fig. 5).

4.3. Shionohira fault hydromechanical response

Fig. 12a, b shows the calculated pressure in the Shionohira fault for different model parameters, during the first step of 7.6 l/min constant flowrate. The model 1 is reproducing reasonably well the injection and the monitoring pressure variations when (1) a high permeable hanging wall (fault western compartment) of 10^{-10} m^2 is considered to figure the high permeability of the sedimentary layers compared to the footwall (eastern compartment) metamorphic rocks, and the fault is affected (2) a 14° constant friction angle and (3) a 12 GPa/m elastic stiffness (Table 2). When no high permeable sedimentary deposits are considered, there is an overestimation of the calculated pressures because pressure cannot be dissipated by leakage into the sedimentary deposits (model 2, Fig. 12 and Table 2) In that case, we observe three slightly different fault hydromechanical responses:

- Model 3 - A low constant friction angle of 10° still overestimates the pressure because it favors a slip patch rather than a large opening patch propagation in the fault. The slip favored on the weak fault induces dilation that progressively dissipates part of the pressure.
- Model 4 - A high fault elastic stiffness of 18 GPa/m limits the initial fault normal opening, showing a large over estimation of injection pressure.
- Model 5 - A slip-weakening friction from an initial peak friction of 18° shows about the same pressure variation that the constant friction fault. This is explained by the fact that most of the friction decrease occurs during the first 10 s of water injection. After 10 s, the friction tends to a residual friction of 13.8° which is close to the low constant 14° friction case, resulting in about the same fault hydromechanical response. To our opinion, this could show that fault remained relatively close to its residual frictional strength and that no friction recovery occurred after the activation by the 2011 Mw 6.7 Fukushima-ken Hamadori earthquake.

In Fig. 12c, d, we compare the calculated fault normal and shear displacements with the ones isolated in the field during the rupture propagation phase, outside the artificial flowrate increase periods (colored segments in Fig. 8). Both constant friction models and the slip-weakening model underestimate the slip measured during the first flow step, and much better match with the slip captured during the following flow steps. The fact that models do not reproduce that first experimental flow step might confirm that the measured signal during this step is influenced by some borehole nearfield complexity that is not considered in the models. Indeed, the model figures the fault as a single discontinuity while borehole observations show that the fault is a thick and complex zone (Fig. 3). During the first cycle, failure may nucleate on some local heterogeneity within the fault zone before organizing along the average fault orientation during the following cycles. Another

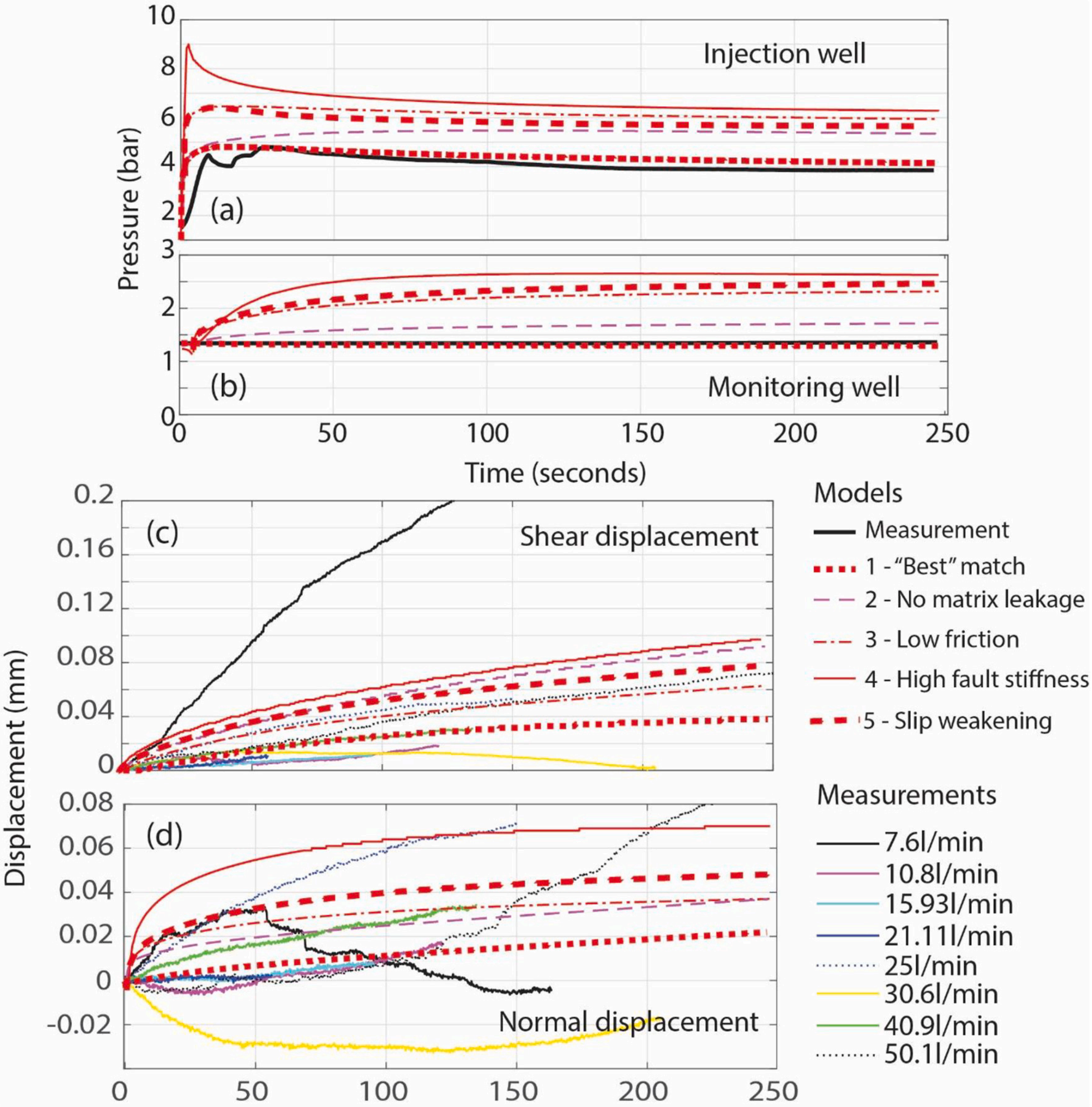

Fig. 12. Shinohira test numerical results (a) Injection pressure (b) Monitoring pressure (c) Fault shear displacement (d) Fault normal displacement.

possibility is that during the first cycle, fault activation mechanism is not pure shear failure. Indeed, Fig. 7 shows that during this cycle, the fault displacement contains a significant component perpendicular to the average fault plane orientation.

A low fault normal opening is calculated in the range of the field measurements during the first 100 s (Fig. 12c). Model 1 with a 10^{-10} m^2 hanging wall permeability best fit with the field measurements captured during the following flow steps. The non-linear slip increase with time is reasonably well reproduced (Fig. 12d). Model 3 with the 10° constant friction angle model and the frictional weakening model 5 overestimate the slip during the first 100 s. The high 18 GPa/m elastic stiffness model 4 overestimates both the normal opening and the fault slip. This is because the higher injection pressure that is required to open the fault is inducing a larger effective normal stress decrease than in the other cases. The result is that, once activated, the fault is opening and slipping significantly more.

4.4. *Itozawa fault (south) hydromechanical response*

Fig. 13 shows that the initiation of the Itozawa fault (South) reactivation during the [15:22–15:41] injection cycle is best reproduced for a set of model parameters including (1) a normal stress on the fault that does not exceed 0.2 MPa, (2) a friction angle of 19° and (3) a cohesion of 0.4×10^6 Pa (red curve corresponding to model 1, Fig. 13a and Table 2). At 700 s, when pressure is increased from 14.1 to 16.3 bar, the model displays a significant increase in fault normal opening to a peak value of the same amplitude as the amount of shear increase. This is followed by an injection pressure decay and a normal closing of the fault while there is no shear displacement. If it reproduces well the pressure at which fault is activated and the general shape of the pressure-displacement signals, the model overestimates the amplitude of the normal displacement peak and the following decay in both pressure and displacement, and it underestimates the amount of shear displacement. At 800 s, pressure is again artificially increased to 15.6 bar, producing the same pressure and displacement response of the fault. In this second fault activation step, there is less overestimation of the normal displacement peak and a much better fit of the injection pressure and the shear displacement variation. Overall, the model 1 restitutes reasonably well the two highly dilatant shear events triggered by two injection pressure increases above 14.1 bars (Fig. 13).

If the normal stress is increased above 0.2 MPa, there is no rupture, and no associated injection pressure drop (magenta curve corresponding

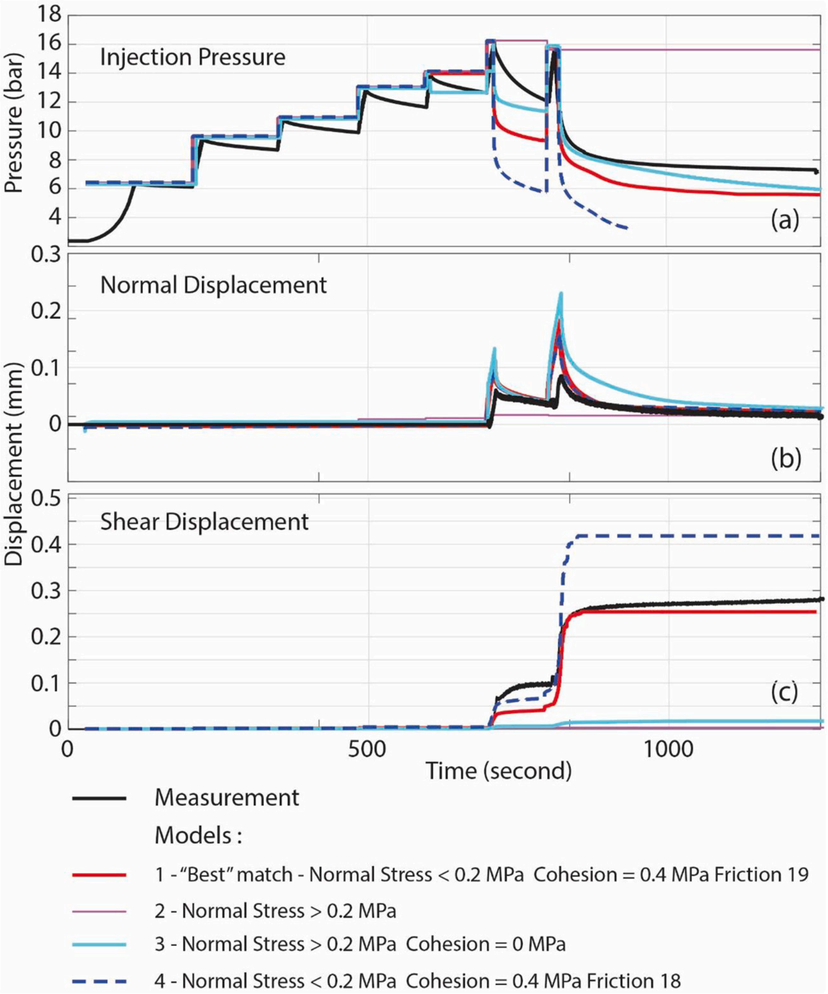

Fig. 13. Minakami-kita [15:22–15:41] test numerical results (a) Injection pressure (b) Fault normal displacement (c) Fault shear displacement.

to model 2, Fig. 13 and Table 2) unless the fault is affected a cohesion of 0 Pa (cyan curve corresponding to model 3, Fig. 13 and Table 2). In that case, the shear displacement is nevertheless highly underestimated, and horizontal minimum and maximum stresses must be set to high and unrealistic values equal to higher than the vertical stress, with $\sigma_h = 0.65$ MPa, $\sigma_H = 0.7$ MPa and $\sigma_v = 6.8$ MPa. If the normal stress does not exceed 0.2 MPa, a slight decrease in the friction angle from 19° to 18° increases the amount of shear (dark blue dashed curve corresponding to model 4, Fig. 13 and Table 2).

We used the same best fit fault properties from model 1, to model the cycle [15:56–16:36] where a constant pressure step injection was conducted with an engine pump, inducing a hydraulic connection with the monitoring borehole (Fig. 14). There is a reasonable match of the fault opening injection pressure and of the following pressure decay until the shut-in at 1011 s (Fig. 14a). The shut-in pressure decay period is much larger in the model than in the field. This is because the calculated injection flow patch reached the model boundaries which are set at the formation pressure of 1.8 bar (at the depth of the injection), and consequently the patch was drained at the boundaries. In the field, there is less hydraulic connection (leakage) between the activated fracture and the surrounding aquifer. The model 1 underestimates the amplitude of the pressure increase at the monitoring well of about 1.3 bars (Fig. 14c). The pressure is varying much faster in the model and the hydraulic connection occurs earlier. In the model 1, there is a large flow injection in the fault as soon as the opening pressure is reached (Fig. 14b). In the field, that large flow variation happens 90 s later (when attempting to increase pressure again) showing that compared to the model the coupling between fault rupture and fluid penetration is much more complex in the field. Such a complexity is strongly affecting the calculated displacements which poorly match the measurements (Fig. 14d, e). With the same fault friction and cohesion as in the initiation cycle [15:22–15:41], both the normal and shear calculated fault displacements are underestimated by a factor of ~3 (blue curve, Fig. 14d, e). Model 5 with a lower friction fault does not significantly increase the calculated displacement (green curve, Fig. 14d, e). In addition, the shape of the shear displacement curve is poorly reproduced.

To better describe these experimental curves, we considered more complex fault activation schemes. First, in model 6, we considered that three fractures instead of one (Fig. 14g), all with the same dip and dip direction, are being activated (red curve, Fig. 14d, e). This is consistent with the geology of the interval which shows several natural planes more or less parallel to the PSZ (Fig. 3c). In that case, the model 6 calculates more displacement amplitude closer to the range of field observations, except that there is no calculated shear decay and that the fault normal closing is overestimated during the shut-in period. Second, in model 7, we considered that, in addition to the reopening of the natural fault, a new fluid driven fracture (i.e., hydrofracture) may have been created (Fig. 14h). Unfortunately, this hypothesis could not be checked after the test because of the injection borehole collapse. We hypothesized that the normal to the hydrofracture plane is oriented parallel to the main displacement trend. In that case, the calculated shear displacement shows a more complex shape closer to the field one during injection and during shut-in (cyan curve, Fig. 14d, e). In that

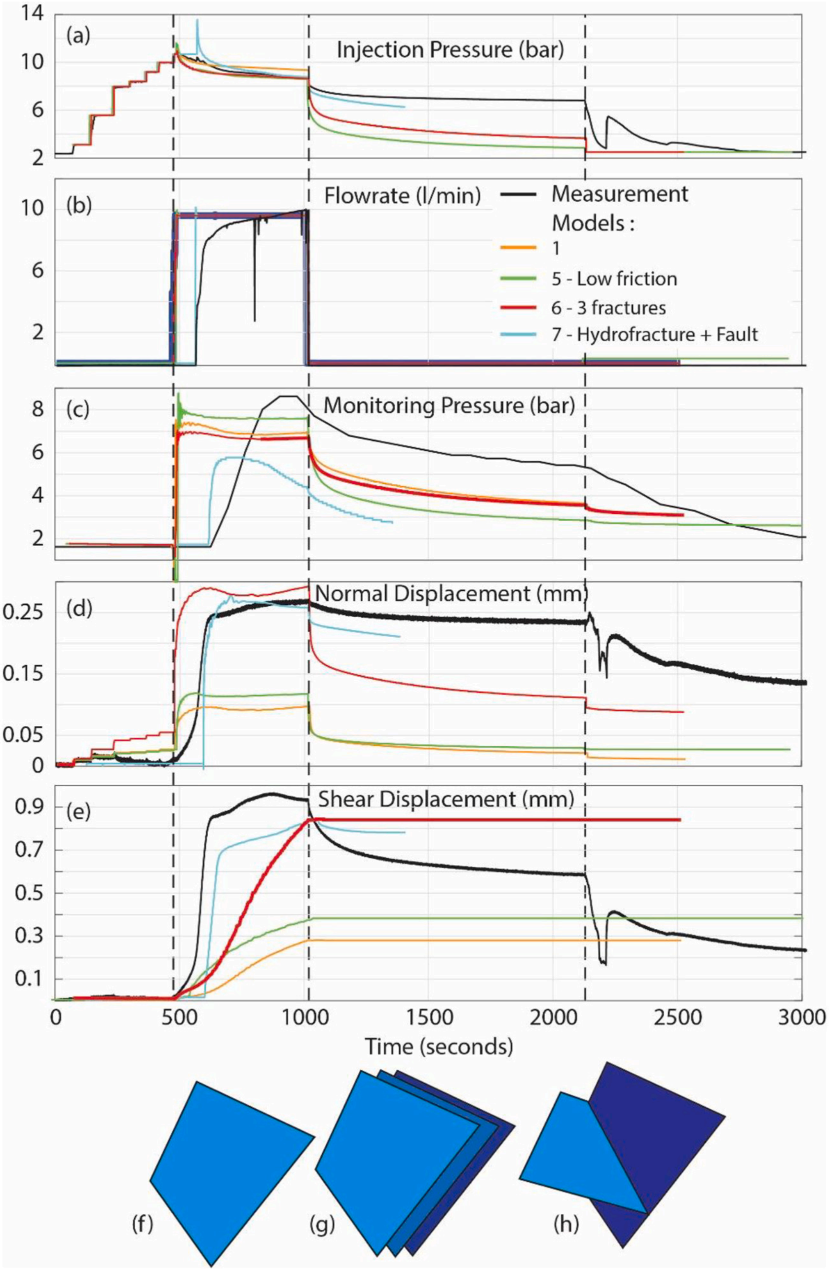

Fig. 14. Minakami-kita [15:56–16:36] test numerical results (a) Injection pressure (b) Flowrate (c) Monitoring pressure (d) Fault normal displacement (e) Fault shear displacement.

second hypothesis, this would show that, during cycle 3, the measured shear displacement is more influenced by the hydrofracture opening than by slip on the PSZ.

5. Discussion

5.1. Comparison of Shinohira and Itozawa fault (south) hydromechanical responses

The numerical analysis shows significantly different hydromechanical reactivation mechanisms between the Shionohira fault and Itozawa fault (south) segments (Fig. 15).

Given the shallow depth of the tests, we calculate that fault rupture propagated to the land surface in both tests (Fig. 15a, b). In the field, rupture reactivation was not observed at the land surface during our tests, except indirectly at Shionohira through the appearance of a water outflow. The fact that rupture is not clearly observed is explained by the simplicity of the model close to the surface where no soil layer was represented. In the field, this layer may have hidden most of the movements which are of infra-millimeter scale as calculated by the models. We may also advocate that there was no instrument to detect such infinitesimal movements at the land surface (which cannot be detected visually).

The reactivation mode is a Coulomb shear failure at Shionohira (Fig. 15c) and a complex tensile failure at Minakami-kita (Fig. 15d). The difference in the rupture modes explains the strong difference observed in the calculated normal and shear displacements on the fault of the two sites (Fig. 15a, b). Shear displacements at Shionohira are about a factor of 10 higher than normal displacements, which is in good accordance with a shear-induced-dilatant rupture (Fig. 15a). Most of the shear measured in the field is explained by slip on the PSZ in the model. Model also shows that leakage into the sandstones of the fault's western

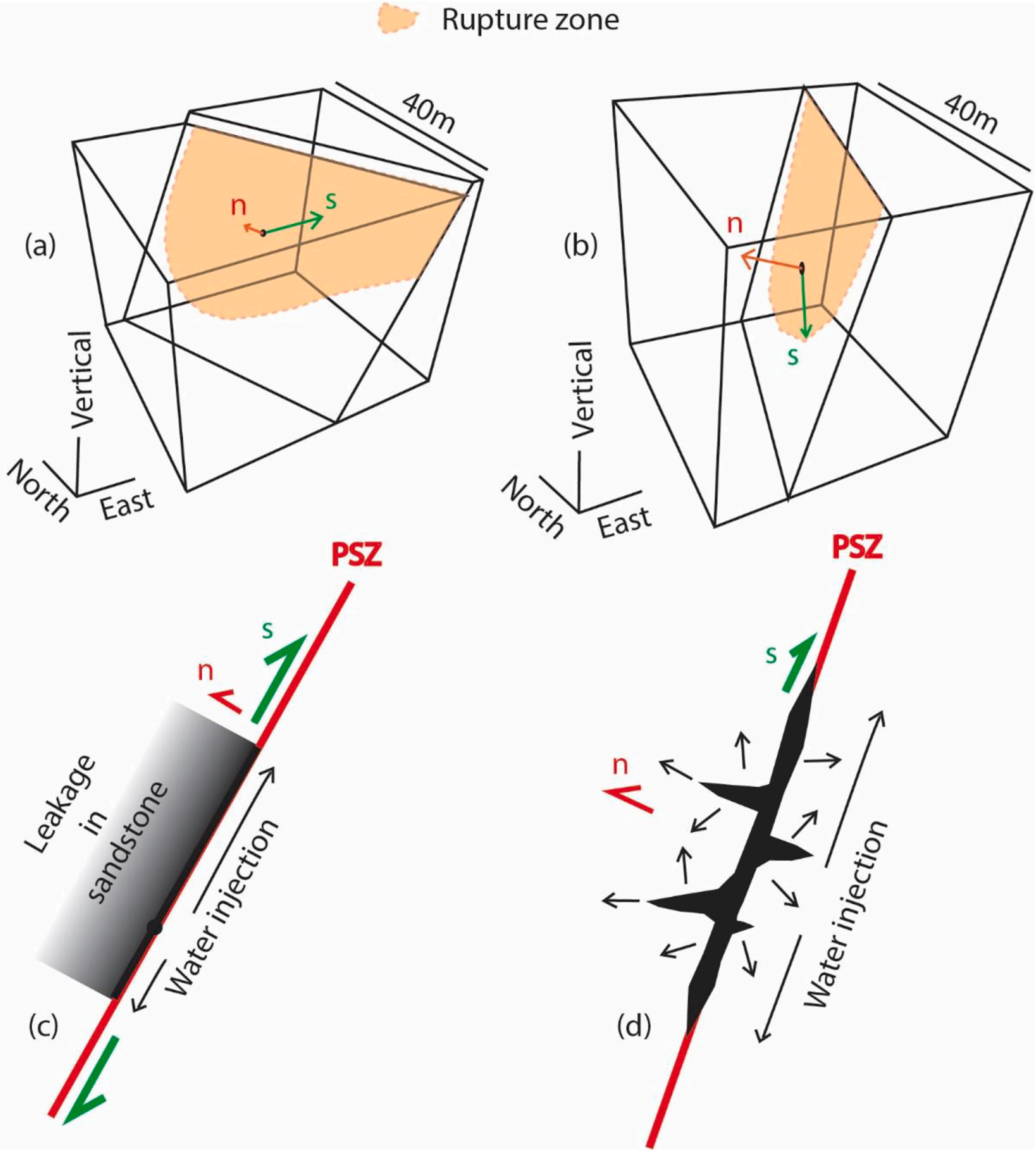

Fig. 15. Rupture mechanisms at the Shionohira and at the Minakami-kita sites. Rupture zone and fault normal (n) and shear (s) displacements calculated at (a) Shionohira and (b) Minakami-kita sites. Interpreted rupture mechanisms at (c) Shionohira and (d) Minakami-kita sites (Injected water is figured in black, PSZ is the Principal Shear Zone).

compartment controls fault pressure, and thus rupture growth (Fig. 15c). At Minakami-kita, shear and normal opening are of the same order of magnitude (Fig. 15b). In addition, model poorly reproduces the displacement curves during the cycle 3 of fault rupture propagation away from the injection borehole. Considering multiple natural planes activation and the creation of fluid driven fractures improved the match of model results to field signals. This is suggesting that the Minakami-kita field shear displacement cannot be explained just by slip on the PSZ (Fig. 15d).

Effective stress variations are thus different between the two sites, and may mainly relate to difference in the fault zone properties rather than to the stress states which are dominated by the shallow depth of the tests. Indeed, thanks to a low static friction angle of 14°and no cohesion, the normal and shear stress variations on the Shionohira fault are small at the end of the test. This is not the case at Minakami-kita where the higher friction of 18°and the cohesion of 0.4 MPa necessitate a larger change in effective stress for the fault to reactivate. At the end of the test, both normal and shear stress fall to almost zero in the rupture patch.

One difficult-to-answer question is whether the Shionohira segment behaved differently because of different fault structure and properties, or if it is the recent rupture hitting the ground surface that refreshed these properties compared to Minakami-kita site. Answering such a question would obviously need repeating the SIMFIP field tests on a larger number of activated and un-activated fault outcrops. The tests presented in this study prove that it is possible since the setting of the tests is relatively easy, involving the drilling of a well and a 1–2 weeks deployment and SIMFIP testing.

5.2. *Inversion of SIMFIP displacements to estimate a deep tectonic fault frictional evolution*

From the field tests forward analyses of the Shionohira test, we get a residual friction coefficient varying of 0.23–0.25 (or ~ 14°friction angle, Table 2). These values are consistent with observations at laboratory scale of friction coefficients of 0.1–0.2 for Shionohira fault wet gouges with 30 wt% of H_2O (Aoki et al., 2015).We then compared the previous forward models described in Section 4 with an inverse approach, in order to explore how the continuously monitored fault shear displacements (slip) can inform on fault friction evolution when the fluid pressure changes in the fault. Following the approach developed in Guglielmi et al. (2015a, 2015b), the fault is represented as a one-dimensional spring-slider model (Fig. 16). To obtain the shear displacement along a fluid-saturated, rate-and-state fault, we solve the following system of coupled equations:

- Rate-and-state friction law:

$$\frac{\tau(\theta, V)}{\sigma_n} = \mu(\theta, V) = \mu_o + a\ln\left(\frac{V}{V_o}\right) + b\ln\left(\frac{V_o\theta}{D_c}\right) \tag{3}$$

- Aging law:

$$\frac{d\theta}{dt} = 1 - \frac{V\theta}{D_c} \tag{4}$$

- Elastic coupling:

$$\frac{d\mu}{dt} = k\left(V_{lp} - V\right) \tag{5}$$

- Fluid pressure:

$$\frac{dp}{dt} = \frac{\left(\frac{\varepsilon}{\theta}\frac{d\theta}{dt}\right) + \left(\frac{kh}{\eta L^2}(p - p_0)\right)}{\phi\left(\beta_\phi + \beta_w\right)} \tag{6}$$

- Shear displacement velocity (Slip velocity):

$$V = V_o exp\left[\frac{\frac{k\left(u_{lp} - u\right)}{\sigma_n - p} - \mu_o - b\ln\left(\frac{V_o\theta}{D_c}\right)}{a}\right] \tag{7}$$

- Shear displacement (Slip):

$$s(t) = V_o\int_0^t exp\left[\frac{\frac{k\left(u_{lp} - u\right)}{\sigma_n - p} - \mu_o - b\ln\left(\frac{V_o\theta}{D_c}\right)}{a}\right] \bullet \Delta t \tag{8}$$

with:

V_{lp} = load-point moving at constant velocity; the displacement of which is u_{lp}

k = stiffness of the spring

V = velocity of the slider; the displacement of which is u

μ = friction coefficient

μ_o = reference friction coefficient corresponding to a reference slip velocity (V_o)

D_c = critical slip distance

a and b = non-dimensional rate-and-state parameters

θ = state variable. At an initial steady state, $\theta_i = D_c/V_{ss}$ where Vss denotes the steady state velocity

σ_n = normal stress

τ = shear stress

p = fluid pressure

t = time

Δt = time step

ε = dilatancy coefficient

ϕ = porosity

k_h = permeability

η = dynamic viscosity of fluid

β_ϕ = pore compressibility

β_w = fluid compressibility

L = layer thickness

V = fault slip velocity

s = fault shear displacement (slip)

We solve with MATLAB the coupled Eqs. ((3)–(6)) to calculate the fault shear displacement velocity and shear displacement (Eqs. (7)–(8)) using a fifth order Runge-Kutta method with error tolerance between 1×10^{-6} and 1×10^{-4}. Then, we invert the model output in an adaptive grid-search approach to obtain the best fit estimate of the rate-and-state friction parameters (μ_o, a-b, D_c, Dieterich, 1979, Ruina, 1983). Here, we set-up the procedure in order to apply a fluid pressure loading in the fault and calculate the fault shear displacement. Applied on a SIMFIP test conducted at 280 m depth in faulted carbonates, the parameters

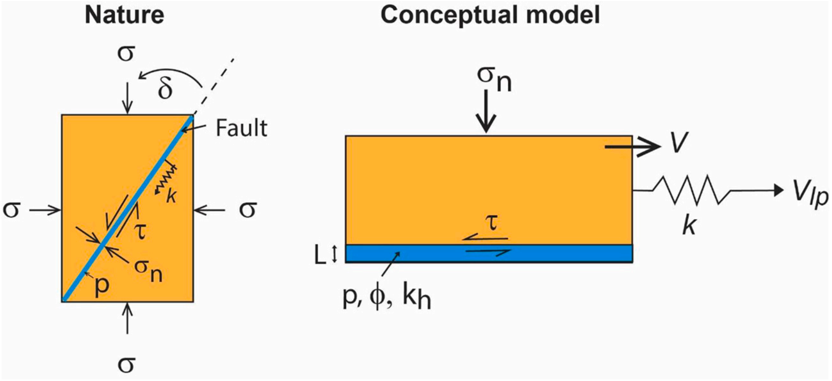

Fig. 16. Conceptual 1D spring-slider model of a fluid-saturated, rate-and-state fault.

estimated from this approach were consistent with values obtained in the laboratory on same carbonate rocks (Cappa et al., 2019).

In the case of the Shionohira test, we used the shear displacement measured on the fault plane during the 50.1 l/min constant flow step (Fig. 8b). We obtain a reasonable fit between the measured data and our calculated displacement and pore pressure variation (Fig. 17a, b), for the following model parameters:

- Normal stress: 5 MPa, Principal Shear Zone Thickness: 20 mm
- Spring stiffness: 0.15 MPa/um, Reference slip velocity: 0.01 μm/s
- Porosity: 0.45, Permeability: $1e^{-18}$ m^2, Dilatancy coefficient: $5\ 10^{-6}$
- $a = 0.001$, $b = 0.008375$, $a\text{-}b = -0.007375$
- $\mu_0 = 0.4$, $D_c = 20$ μm

We get a reasonable restitution of the shear displacement variation and amplitude which shows that a velocity dependent friction law can be applied to describe the Shionohira fault slip variation. On the contrary, Fig. 17c, d show that we get a poor match to the field data of the Minakami-kita cycle 1 test, This supports what was estimated from the forward three-dimensional analyses that a much more complex reactivation of the fault occurred at this site. Hybrid modes of rupture may thus explain the measured shear rather than pure slip on the PSZ.

At the Shionohira site, we calculate a and b values of 0.001 and 0.008375, respectively. This gives $a\text{-}b = -0.007375$ showing that the PSZ tested at Shionohira is slightly rate weakening, considering the relatively slow velocity of 20–33.7 μm/s of the field tests. We get a slight friction coefficient variation of ~0.02 from the rate-and-state friction inverse analyses (Fig. 17a). In the Minakami-kita test, the best case scenario remains far from the data. It corresponds to the following model parameters, $a = 0.001$, $b = 0.00675$, $a\text{-}b = -0.00575$, $\mu_0 = 0.4$, $D_c = 10$ μm. The friction coefficient variation does not explain the measured displacements (Fig. 17c).

At the Shionohira site, our field observations are also consistent with laboratory data that showed a velocity dependence of gouge friction above the sliding velocity of 21 μm/s. Nevertheless, a velocity strengthening regime was identified between 21 μm/s and 21 mm/s, while we identify a velocity weakening of the PSZ in this range of velocities. Velocity weakening is clearly observed in the laboratory above 21 mm/s. This difference might come from the relatively different experimental conditions between the field SIMFIP test and the laboratory tests. Indeed, using advanced fully coupled hydromechanical modeling, Cappa et al. (2019) showed that similar SIMFIP field displacements could be modeled either with a rate-weakening or a rate-strengthening behavior using parameters in the range of the values estimated in the laboratory. The reason is that they identified that the injection zone where there is the highest pressure may experience rate strengthening while at and beyond the tip of the high-pressure patch there may be rate weakening in the activated fault. In a SIMFIP test, the

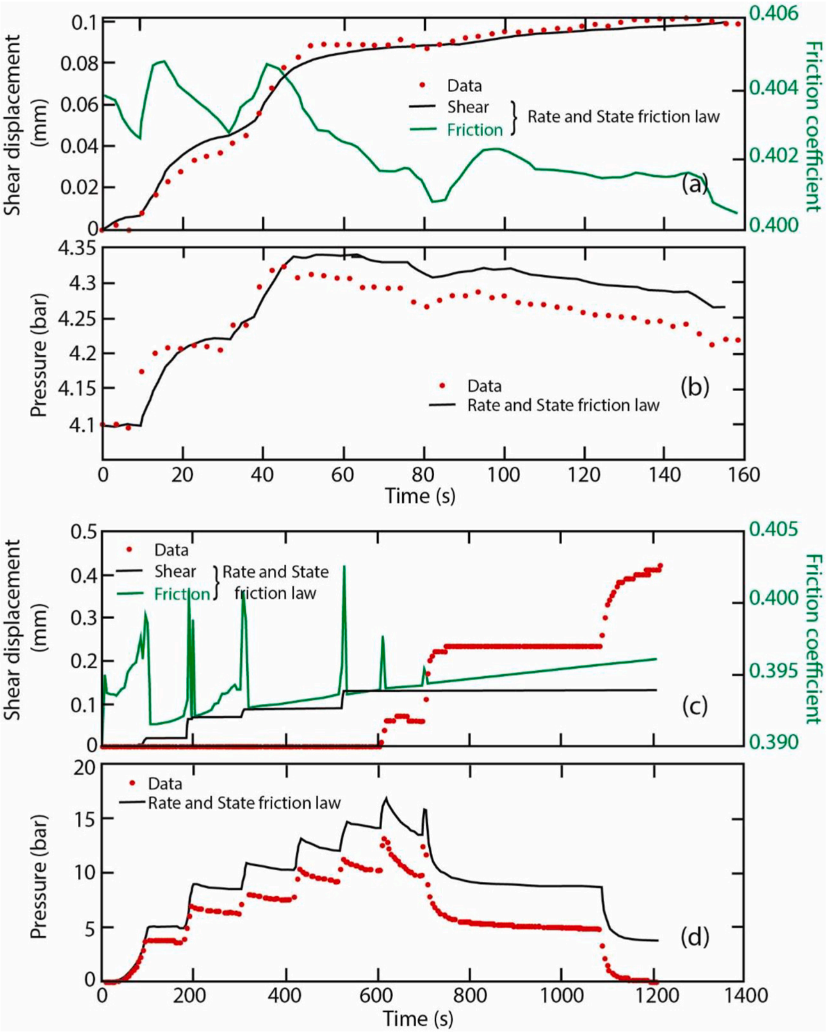

Fig. 17. Results of the spring-slider model used to invert fault Rate and State frictional properties. Shionohira test - (a) measured shear compared to calculated shear displacement and friction. (b) measured and calculated pore pressure. Minakami test - (c) measured shear compared to calculated shear displacement and friction and (d) measured and calculated pore pressure.

borehole displacements capture both borehole near and far field effects with time while these "contrasted" effects are obviously much better isolated at laboratory scale.

Finally, the key result is that SIMFIP tests allow exploring which friction law is potentially the best to describe fault rupture, giving an in-situ fault scale estimate of the fault frictional strength in the case of the recently ruptured Shionohira fault. It appears that (i) the fault static friction is low and consistent with laboratory scale estimations and (ii) during slip there is a slight tendency to frictional weakening that can be described using a rate and state friction law. These information are consistent with the triggering of the April 11, 2011 Fukushima-ken Hamadori Earthquake in some deeper fault conditions.

5.3. Implications of the approach in the in-situ estimation of the fault activation modes

SIMFIP field tests allow providing activation mechanisms of surface fault ruptures and, thanks to the continuous fault displacement data, they allow a realistic tuning of fully coupled hydromechanical numerical models from the in-situ estimation of fault friction, cohesion, elastic stiffness and hydraulic conductivity. This is an improvement since current numerical simulations of surface rupture are usually "only" verified from laboratory scale-model tests (Anastasopoulos and Gazetas, 2007). We observe that complex ruptures can occur, involving variations in rock properties, non-uniform local stresses and coupled effects between the shallow aquifer and the fault zone activation. Indeed, the Shinohira test shows the influence of the hanging wall high permeability, the stress perturbation by the nearby valley and rate-weakening fault frictional behavior in modulating the rupture propagation. These information complement numerical models that usually use a Mohr–Coulomb constitutive model for rupture initiation followed by a strain-softening friction model to describe the rupture growth (Anastasopoulos et al., 2007) and highlight the topographic free surface effect on rupture (Bransby et al., 2008). The Minakami-kita test provides an even more complex scenario constrained by the fault zone initial low permeability and cohesive strength that influence slip initiation on the identified PSZ followed by a failure propagation on other existing or newly created fractures within the fault zone. These scenarios that are here directly probed in situ are invoked as reasons for the surface rupture to occur in a previously ruptured zone or in a newly unruptured area (Gudmundsson et al., 2010). The protocol developed in this study is providing an in situ estimation of residual primary fault properties and rupture evolution that are key to estimate the potential for displacement that could be induced on a small fault segment by a designed synthetic earthquake. This protocol can thus contribute to improve methods to assess the safety of dam or nuclear waste disposal subject to earthquake such as the one proposed by Fälth et al. (2015).

6. Conclusion

The shallow, 10–30 m deep, SIMFIP tests for fault reactivation by fluid injection identified in-situ two contrasted fault hydromechanical responses. The Shionohira surface rupture, recently activated during the 2011 M_W 6.7 Fukushima-ken Hamadori earthquake, displayed a dilatant slip response to hydraulic tests while the un-activated Itosawa fault (South) displayed a complex hybrid response related to both a higher frictional and cohesive strengths of the fault. The analysis of the induced Shionohira slip event showed that it could be modeled as a Coulomb rupture with an eventual dependency of friction on slip velocity, in good accordance with rate-and-state friction data obtained in the laboratory on Shinohira gouge samples. The tested Shionohira fault segment thus displays overall weaker properties than the Itosawa fault segment.

Finally, the SIMFIP tool used in this study can be deployed deeper (0.5–1.5 km, see for ex. Guglielmi et al., 2021) to assess how a small fault segment may be triggered by a design earthquake, and what could be the maximum slip amount to consider for the safety assessment of structures such as nuclear waste repositories and dams.

Declaration of Competing Interest

The authors declare that they have no known competing financial interests or personal relationships that could have appeared to influence the work reported in this paper.

Acknowledgements

The authors thank M. Kametaka, E. Iwasaki, and H. Wakahama of DiaConsultants for drilling and assistance in data acquisitions. Weacknowledge the editor Ling Chen and the two anonymous reviewers for theirthoughtful comments.

References

Aki, K., 1995. Interrelation between fault zone structure and earthquake processes. Pure Appl. Geophys. 145, 647–676.
Anastasopoulos, I., Gazetas, G., 2007. Foundation–structure systems over a rupturing normal fault: part I. Observations after the Kocaeli 1999 earthquake. Bull. Earthq. Eng. 5, 253–275.
Anastasopoulos, I., Gazetas, G., Bransby, M.F., 2007. Fault rupture propagation through sand: fnite element analysis and validation through centrifuge experiments. J. Geotech. Geoenviron. Eng. 133, 943–958.
Angelier, J., 1979. Determination of the mean principal directions of stresses for a given fault population. Tectonophysics 56 (3-4), T17–T26.
Aoki, K., Seshimo, K., Tanaka, Y., Niwa, M., Kametaka, M., Sakai, T., Shimamoto, T., 2015. Frictional properties of Shionohira Fault Gouge of Fukushima, Japan. In: AGU Fall Meeting, San Francisco, Poster T51A-2843.
Avar, B.B., Hudyma, N.W., 2019. Earthquake Surface Rupture: a brief survey on interdisciplinary research and practice from geology to geotechnical engineering. Rock Mech. Rock. Eng. 52, 5259–5281. https://doi.org/10.1007/s00603-019-02006-0.
Barton, C.A., Zoback, M.D., 1994. Stress perturbations associated with active faults penetrated by boreholes: possible evidence for nearcomplete stress drop and a new technique for stress magnitude measurement. J. Geophys. Res. 99, 9373–9390. https://doi.org/10.1029/93JB03359.
Bott, M.H.P., 1959. The mechanics of oblique slip faulting. Geol. Mag. 96 (2), 109–117.
Bransby, M.F., Davies, M.C.R., El Nahas, A., Nagaoka, S., 2008. Centrifuge modelling of reverse fault–foundation interaction. Bull. Earthq. Eng. 6, 607–628.
Cappa, F., Scuderi, M.M., Collettini, M., Guglielmi, Y., Avouac, J.P., 2019. Stabilization of fault slip by fluid injection in the laboratory and in-situ. Sci. Adv. 5 https://doi.org/10.1126/sciadv.aau4065 eaau4065.
Detournay, E., 1980. Hydraulic conductivity of closed rock fracture: an experimental and analytical study. In: Proceedings of the 13th Canadian Rock Mechanics Symposium, pp. 168–173.
Dieterich, J.H., 1979. Modeling of rock friction, 1. Experimental results and constitutive equations. J. Geophys. Res. 84, 2161–2168.
Dolan, J.F., Haravitch, B.D., 2014. How well do surface slip measurements track slip at depth in large strike-slip earthquakes? The importance of fault structural maturity in controlling on-fault slip versus off-fault surface deformation. Earth Planet. Sci. Lett. 388, 38–47.
Fälth, B., Hökmark, H., Lund, B., Mai, P.M., Roberts, R., Munier, R., 2015. Simulating earthquake rupture and off-fault fracture response: application to the safety assessment of the swedish nuclear waste repository. Bull. Seismol. Soc. Am. 105 (1), 134–151. February 2015. https://doi.org/10.1785/0120140090.
Gudmundsson, A., Simmenes, T.H., Larsen, B., Philipp, S.L., 2010. Effects of internal structure and local stresses on fracture propagation, defection, and arrest in fault zones. J. Struct. Geol. 32, 1643–1655.
Guglielmi, Y., Cappa, F., Lançon, H., Janowcsyk, J.B., Rutqvist, J., Tsang, C.-F., Wang, J. S.Y., 2014. ISRM suggested method for Step-Rate Injection Method for Fracture In-Situ Properties (SIMFIP): using a 3-components borehole deformation sensor. Rock Mech. Rock. Eng. 47 (1), 303–311. https://doi.org/10.1007/s00603-013-0517-1.
Guglielmi, Y., Cappa, F., Avouac, J.P., Henry, P., Elsworth, D., 2015a. Seismicity triggered by fluid-injection-induced aseismic slip. Science 348 (6240), 1224–1226. https://doi.org/10.1126/science.aab0476.
Guglielmi, Y., Elsworth, D., Cappa, F., Henry, P., Gout, C., Dick, P., Durand, J., 2015b. In Situ observations on the coupling between hydraulic diffusivity and displacements during fault reactivation in shales. J. Geophys. Res. Solid Earth 120. https://doi.org/10.10002/2015JB012158.
Guglielmi, Y., Nussbaum, C., Rutqvist, J., Cappa, F., Jeanne, P., Birkholzer, J., 2020. Estimating perturbed stress from 3-D borehole displacements induced by fluid injection in fractured or faulted shales. Geophys. J. Int. 221, 1684–1695. https://doi.org/10.1093/gji/ggaa103.
Guglielmi, Y., Cook, P., Soom, F., Schoenball, M., Dobson, P., Kneafsey, T., 2021. In Situ continuous monitoring of borehole displacements induced by stimulated hydrofracture growth. Geophys. Res. Lett. 48 (4).
Hart, E.W., Bryant, W.A., Treiman, J.A., 1993. Surface faulting associated with the June 1992 Landers earthquake, California. Calif. Geol. 46, 10–16.

Ishiyama, T., Sato, H., Ito, T., Matsudo, N., Echigo, T., Kato, N., Imaizumi, T., 2011. The Surface Earthquake Fault of the 11 April 2011 Earthquake in Hamadoori Fukushima Pref. Report 2: 11th to 13th April field survey report. https://www.eri.utokyo.ac.jp/TOPICS_OLD/outreach/eqvolc/201103_tohoku/eng/hamadoori/#report2.

Itasca Consulting Group, 2016. 3DEC, 3-Dimensional Distinct Element Code. Itasca Consulting Group, Minneapolis, MN.

Jeanne, P., Guglielmi, Y., Cappa, F., Rinaldi, A.P., Rutqvist, J., 2014. Effects of lateral properties variations on fault zones reactivation by fluid pressurization: application to CO2 pressurizations effects of mature and undetectable fault zones. J. Struct. Geol. 62, 97–108.

Jeanne, P., Guglielmi, Y., Rutqvist, J., Nussbaum, C., Birkholzer, J., 2017. Field characterization of elastic properties across a fault zone reactivated by fluid injection. J. Geophys. Res. Solid Earth 122. https://doi.org/10.1002/2017JB014384.

Kakurina, M., Guglielmi, Y., Nussbaum, C., Valley, B., 2019. Slip perturbation during fault reactivation by a fluid injection. Tectonophysics 757, 140–152.

Kakurina, M., Guglielmi, Y., Nussbaum, C., Valley, B., 2020. In situ direct displacement information fault reactivation during fluid injection. Rock Mech. Rock. Eng. 53, 4313–4328.

Kato, A., Sakai, S., Obara, K., 2011. A normal-faulting seismic sequence triggered by the 2011 off the Pacific coast of Tohoku earthquake: wholesale stress regime changes in the upper plate. Earth Planets Space 63, 745–748. https://doi.org/10.5047/eps.2011.06.014.

Kuwahara, Y., Ito, H., Kiguchi, T., 1991. Comparison between natural fractures and fracture parameters derived from VSP. Geophys. J. Int. 107, 475–483.

Lecampion, B., Desroches, J., Jeffrey, R.G., Bunger, A.P., 2017. Experiments versus theory for the initiation and propagation of radial hydraulic fractures in low-permeability materials. J. Geophys. Res. Solid Earth 122, 1239–1263. https://doi.org/10.1002/2016JB013183.

Lienkaemper, J., Borchardt, J., Lisowski, M., 1991. Historic creep rate and potential for seismic slip along the Hayward fault, California. J. Geophys. Res. 96 (B11), 18,261–18,283.

Mitchell, T.M., Faulkner, D.R., 2009. The nature and origin of off-fault damage surrounding strike-slip fault zones with a wide range of displacements: a field study from the Atacama fault zone, northern Chile. J. Struct. Geol. 31, 802e816.

Nakata, T., Imaizumi, T. (Eds.), 2002. Digital Active Fault Map of Japan. Univ. Tokyo Press, Tokyo. DVD and 66p.

Noda, H., Lapusta, N., 2013. Stable creeping fault segments can become destructive as a result of dynamic weakening. Letter Nature 493, 518–522.

Otsubo, M., Shigematsu, N., Takahashi, M., Azuma, T., Imanishi, K., Ando, R., 2013. Slickenlines on fault scarps caused by an earthquake in Iwaki-city (Fukushima Prefecture, Japan) on 11 April 2011. J. Geol. Soc. Jpn. 119 (9).

Research Group for Active Faults in Japan, 1991. Active Faults in Japan, Sheet Maps and Inventories, Revised ed. Univ. Tokyo Press, Tokyo. 437p.

Ruina, A.L., 1983. Slip instability and state variable friction laws. J. Geophys. Res. 88, 359–370.

Scholz, C.H., 1998. Earthquakes and friction laws. Nature 391, 37–42.

Seshimo, K., Aoki, K., Tanaka, Y., Niwa, M., Kametaka, M., Sakai, T., Tanaka, Y., 2015. The properties of fault zone and fault activity of Shionohira Fault, Fukushima, Japan. In: AGU Fall Meeting, San Francisco, Poster T51A-2864.

Tanaka, M., Asano, K., Iwata, T., Kubo, Hisahiko, 2014. Source rupture process of the 2011 Fukushima-ken Hamadori earthquake: how did the two subparallel faults rupture? Earth Planets Space 66, 101.

Toda, S., Tsutsumi, H., 2013. Simultaneous reactivation of two, subparallel, inland normal faults during the Mw 6.6 11 April 2011 Iwaki earthquake triggered by the Mw 9.0 Tohoku-oki, Japan earthquake. Bull. Seismol. Soc. Am. 103, 1584–1602. https://doi.org/10.1785/0120120281.

Wallace, R.E., 1951. Geometry of shearing stress and relation to faulting. J. Geol. 59 (2), 118–130.

Witherspoon, P.A., Wang, J.S.Y., Iwai, K., Gale, J.E., 1980. Validity of cubic law for fluid flow in a deformable rock fracture. Water Resour. Res. 16 (6), 1016–1024.

Yamaji, A., 2003. Are the solutions of stress inversion correct? Visualization of their reliability and the separation of stresses from heterogeneous fault-slip data. J. Struct. Geol. 25, 241–252.

Yoshida, K., Hasegawa, A., Okada, T., 2015. Spatially heterogeneous stress field in the source area of the 2011 Mw 6.6 Fukushima-Hamadori earthquake, NE Japan, probably caused by static stress change. Geophys. J. Int. 201, 1062–1071.